this effect, indicating that the reduction in T_2 is due to low-frequency noise, which we attribute to magnetic domain noise of the tip material. We expect that this effect can be mitigated using alternative tip materials such as rare earth ferromagnets (*27*). The coupling strength can be further improved by using customized nanoresonators with a larger zero-point motion. Using state-of-the-art nanofabrication techniques, resonators with $Q > 10^6$, $\omega_r/2\pi \sim 1$ MHz (*28*), $G_m \sim 10^5$ T/m, and a coupling strength of $\lambda/2\pi \sim 10$ kHz can be fabricated (*4*), which, together with extended coherence times in isotopically purified diamond of $T_2 > 2$ ms (*29*) and faster pulse sequences with $N \sim 136$ pulses (*23*), yield a projected sensitivity of $\eta < 1$ phonon/$\sqrt{\text{Hz}}$. Combined with recently demonstrated single-shot spin readout (*30*), this raises the intriguing prospect of using a single NV center to sense mechanical motion at the scale of zero-point fluctuations in a single shot.

To assess the feasibility of sensing zero-point motion (Fig. 4A), we assume that the resonator is actively cooled near its motional ground state, using either the spin (*4*) or an additional system such as an optical or microwave cavity (*12*, *13*). Such cooling schemes are always accompanied by a decreased effective mechanical quality factor, $Q_{\text{eff}} = Q/\overline{n}_{\text{env}}$, where $\overline{n}_{\text{env}}$ is the phonon occupation number at the temperature of the surrounding environment. Inserting $\overline{n}_{\text{th}} = 0$ and $W = 2Q_{\text{eff}}/N$ into Eq. 1, a near maximal signal $S \sim 1/2$ is obtained, provided that $C = \lambda^2 Q_{\text{eff}} \tilde{T}_2/\omega_r > 1$, where $\tilde{T}_2 = T_2 N^{2/3}$ is the extended spin-coherence time due to dynamical decoupling (*23*). This is verified in Fig. 4B, which demonstrates that for a wide range of realistic parameters with $C > 1$, the zero-point motion of the resonator results in $S \sim 1/2$. The parameter C is a fundamental quantity in the physics of spin-phonon interactions. In direct analogy to the so-called cooperativity in cQED, $C > 1$ marks the onset of coherent quantum effects in a coupled spin-phonon system. Taking the optimized but realistic values $\lambda/2\pi = 10$ kHz, $T_2 = 1$ ms, $Q = 10^6$, $\omega_r/2\pi = 1$ MHz, and $N = 160$ pulses, we find that $C \sim 35$ can be reached at an environmental temperature of $T = 4$ K. Besides detection of zero-point motion, entering this regime could also enable coherent, long-range interactions between individual spins mediated by a mechanical resonator (*17*), which are of great interest for developing scalable, spin-based quantum information systems. Furthermore, by operating at lower environmental temperatures of $T \sim 100$ mK, it becomes possible to use the spin to cool the resonator down to its ground state (*4*) and to engineer quantum superpositions of mechanical motion, which could be read out using a coherent detection scheme like the one we present in this work.

The above considerations indicate that our approach provides an experimentally feasible route toward reaching strong coupling between single phonons and spins. Potential applications ranging from the creation and detection of quantum states of mechanical motion and the realization of quantum spin transducers to novel approaches for nanoscale sensing and readout (*19*, *20*) can be foreseen.

References and Notes

1. M. Scully, M. Zubairy, *Quantum Optics* (Cambridge Univ. Press, Cambridge, 1997).
2. S. Haroche, J. Raimond, *Exploring the Quantum: Atoms, Cavities, and Photons* (Oxford Univ. Press, New York, 2006).
3. R. J. Schoelkopf, S. M. Girvin, *Nature* **451**, 664 (2008).
4. P. Rabl *et al.*, *Phys. Rev. B* **79**, 041302 (2009).
5. P. Treutlein, D. Hunger, S. Camerer, T. W. Hänsch, J. Reichel, *Phys. Rev. Lett.* **99**, 140403 (2007).
6. F. Xue, L. Zhong, Y. Li, C. P. Sun, *Phys. Rev. B* **75**, 033407 (2007).
7. I. Bargatin, M. L. Roukes, *Phys. Rev. Lett.* **91**, 138302 (2003).
8. T. J. Kippenberg, K. J. Vahala, *Science* **321**, 1172 (2008).
9. G. A. Steele *et al.*, *Science* **325**, 1103 (2009).
10. D. Hunger *et al.*, *Phys. Rev. Lett.* **104**, 143002 (2010).
11. A. D. O'Connell *et al.*, *Nature* **464**, 697 (2010).
12. J. D. Teufel *et al.*, *Nature* **475**, 359 (2011).
13. J. Chan *et al.*, *Nature* **478**, 89 (2011).
14. M. D. LaHaye, J. Suh, P. M. Echternach, K. C. Schwab, M. L. Roukes, *Nature* **459**, 960 (2009).
15. O. Arcizet *et al.*, *Nat. Phys.* **7**, 879 (2011).
16. D. Rugar, R. Budakian, H. J. Mamin, B. W. Chui, *Nature* **430**, 329 (2004).
17. P. Rabl *et al.*, *Nat. Phys.* **6**, 602 (2010).
18. G. Balasubramanian *et al.*, *Nature* **455**, 648 (2008).
19. M. Grinolds *et al.*, *Nat. Phys.* **7**, 687 (2011).
20. C. Degen, *Appl. Phys. Lett.* **92**, 243111 (2008).
21. S. Kotler, N. Akerman, Y. Glickman, A. Keselman, R. Ozeri, *Nature* **473**, 61 (2011).
22. J. R. Maze *et al.*, *Nature* **455**, 644 (2008).
23. G. de Lange, Z. H. Wang, D. Ristè, V. V. Dobrovitski, R. Hanson, *Science* **330**, 60 (2010).
24. Materials and methods are available as supporting material on *Science* Online.
25. J. Taylor *et al.*, *Nat. Phys.* **4**, 810 (2008).
26. L. Childress *et al.*, *Science* **314**, 281 (2006).
27. B. C. Stipe, H. J. Mamin, T. D. Stowe, T. W. Kenny, D. Rugar, *Phys. Rev. Lett.* **86**, 2874 (2001).
28. S. S. Verbridge, H. G. Craighead, J. M. Parpia, *Appl. Phys. Lett.* **92**, 013112 (2008).
29. G. Balasubramanian *et al.*, *Nat. Mater.* **8**, 383 (2009).
30. L. Robledo *et al.*, *Nature* **477**, 574 (2011).

Acknowledgments: We thank T. Baart, M. Grinolds, P. Maletinsky, S. Hong, and A. Yacoby for stimulating discussions and R. Ilic, F. Koppens, and A. Zibrov for early contributions to the experiment. This work was supported in part by the NSF, the Center for Ultracold Atoms, the Air Force Office of Scientific Research Multidisciplinary University Research Initiative, the Defense Advanced Research Projects Agency Quantum-Assisted Sensing and Readout, the European Union (EU) Diamond-Based Atomic Nanotechnologies, and the Packard Foundation. S.K. acknowledges support by the U.S. Department of Defense through the National Defense Science and Engineering Graduate Program and the NSF through the Graduate Research Fellowship Program under grant no. DGE-1144152. Q.U. acknowledges support from Deutschen Forschungsgemeinschaft, and P.R. acknowledges support by the EU network Atomic Quantum Technologies Integrating Project and the Austrian Science Fund (FWF) through Sonderforschungsbereich FOQUS and the START grant Y 591-N16.

Supporting Online Material

www.sciencemag.org/cgi/content/full/science.1216821/DC1
Materials and Methods
SOM Text
Figs. S1 to S3
Tables S1 and S2
References

18 November 2011; accepted 8 February 2012
Published online 23 February 2012;
10.1126/science.1216821

Hydrocarbon Separations in a Metal-Organic Framework with Open Iron(II) Coordination Sites

Eric D. Bloch,[1] Wendy L. Queen,[1,2] Rajamani Krishna,[3] Joseph M. Zadrozny,[1] Craig M. Brown,[2,4] Jeffrey R. Long[1,5]*

The energy costs associated with large-scale industrial separation of light hydrocarbons by cryogenic distillation could potentially be lowered through development of selective solid adsorbents that operate at higher temperatures. Here, the metal-organic framework $Fe_2(dobdc)$ ($dobdc^{4-}$: 2,5-dioxido-1,4-benzenedicarboxylate) is demonstrated to exhibit excellent performance characteristics for separation of ethylene/ethane and propylene/propane mixtures at 318 kelvin. Breakthrough data obtained for these mixtures provide experimental validation of simulations, which in turn predict high selectivities and capacities of this material for the fractionation of methane/ethane/ethylene/acetylene mixtures, removal of acetylene impurities from ethylene, and membrane-based olefin/paraffin separations. Neutron powder diffraction data confirm a side-on coordination of acetylene, ethylene, and propylene at the iron(II) centers, while also providing solid-state structural characterization of the much weaker interactions of ethane and propane with the metal.

As a consequence of the similar sizes and volatilities of the molecules, separations of olefin/paraffin mixtures, such as ethylene/ethane and propylene/propane, must currently be performed at low temperatures and high pressures and are among the most energy-intensive separations carried out at large scale in the chemical industry (*1*). Because these gas mixtures are produced by cracking long-chain hydrocarbons at elevated temperatures, a substantial energy penalty arises from cooling the gases to the low temperatures required for distillation. Thus, tremendous energy savings could be realized if materials enabling the efficient separation of olefins and paraffins at higher temperatures (than currently used in distillation) and atmo-

spheric pressure were achieved. Competing approaches toward this end include membrane designs (*2*) and organic solvent-based sorbents (*3*), as well as porous solid adsorbents featuring selective chemical interactions with the carbon-carbon double bond in olefins. In this latter category, metal-organic frameworks (MOFs), which offer high surface areas, adjustable pore dimensions, and chemical tunability, have received considerable attention as adsorbents in gas storage and gas separation applications, with particular emphasis on the dense storage of methane (*4*, *5*) and hydrogen (*6*, *7*) and on the efficient removal of carbon dioxide from flue gas (*8*) and natural gas deposits (*9*, *10*). More recently, the potential utility of these porous structures for the separation of hydrocarbon mixtures has been exposed (*11*–*15*), specifically for the separation of ethylene/ethane and propylene/propane mixtures. Herein, we show that Fe_2(dobdc), a metal-organic framework with exposed iron(II) coordination sites exhibiting high olefin/paraffin selectivities, can be used for the separation of ethylene/ethane and propylene/propane. Furthermore, simulations that are validated by the experimental work presented here allow us to predict that this framework may be further capable of removing acetylene from the ethylene produced by a naphtha cracker and fractionating a methane/ethane/ethylene/acetylene mixture into its pure components. These simulations further predict that Fe_2(dobdc) exhibits higher adsorption selectivities and hydrocarbon separation capacity than a number of recently reported solid adsorbents.

The redox-active metal-organic framework Fe_2(dobdc) (dobdc^{4-} : 2,5-dioxido-1,4-benzenedicarboxylate), also referred to as Fe-MOF-74 or CPO-27-Fe, was selected for testing in separating olefin/paraffin mixtures owing to its previously demonstrated ability to bind O_2 at the iron centers in a side-on manner (*16*). This framework displays a Brunauer-Emmett-Teller surface area of 1350 m^2/g and 11 Å–wide channels lined with square pyramidal Fe^{2+} cations, each with an open coordination site accessible to incoming adsorbate molecules (Fig. 1). With a compact tetra-anionic bridging ligand, the structure features an extremely high surface density of 2.9 Fe^{II} coordination sites available per 100 $Å^2$ on its surface, with spacings of just 6.84(1) and 8.98(2) Å between iron atoms along and around a channel, respectively. Thus, it appears to provide a near-optimal platform for the high-capacity adsorption of small olefins, such as ethylene and propylene. Furthermore, the Mg^{2+} or Co^{2+} analogs of this structure type have recently been shown to display selective adsorption for olefins over paraffins (*17*, *18*). The higher surface area and softer metal character of Fe_2(dobdc) as compared to the recently reported materials should lend both higher selectivity and capacity to the iron(II) framework.

To investigate the ability of Fe_2(dobdc) to adsorb light hydrocarbons, pure component equilibrium adsorption isotherms for methane, ethane, ethylene, acetylene, propane, and propylene were measured at 318, 333, and 353 K. Figure 2 shows the data obtained at 318 K, with the remaining data presented in fig. S1. As evidenced by the initial steep rise in the isotherms, Fe_2(dobdc) displays a strong affinity for the unsaturated hydrocarbons acetylene, ethylene, and propylene. Additionally, the uptake of these gases at 1 bar approaches the stoichiometric quantity expected if one gas molecule is adsorbed per iron(II) center. The propane and ethane adsorption capacities under these conditions, although lower than those of their unsaturated counterparts, are both considerably higher than observed for methane, which has a lower polarizability and a smaller kinetic diameter. Importantly, all of the isotherms are completely reversible and exhibit no hysteresis. Further equilibrium adsorption experiments at 318 K (fig. S2) indicate no loss in olefin uptake capacity over 15 ethylene adsorption/desorption cycles. Additionally, no loss in propylene uptake was observed after 40 adsorption/desorption cycles, as verified by thermogravimetric analysis (fig. S2).

Neutron powder diffraction experiments were carried out to determine the nature of the interactions of these adsorbate molecules within Fe_2(dobdc). In a typical experiment, Fe_2(dobdc) was dosed with deuterated gas at 300 K and cooled to 4 K for data collection. Rietveld refinements were performed against these data to provide the structural models presented in Fig. 1. We recently employed this technique to investigate the coordination of dioxygen to the iron centers of this material (*16*). Analogous to these previous results, only one adsorption site is apparent, corresponding to the open coordination site of the exposed Fe^{2+} cations, upon dosing substoichiometric equivalents of gas per framework iron. The unsaturated hydrocarbons acetylene, ethylene, and propylene indeed display the anticipated side-on binding modes, with Fe-C distances lying in the range 2.42(2) to 2.60(2) Å. These distances are sub-

[1]Department of Chemistry, University of California, Berkeley, CA 94720, USA. [2]Center for Neutron Research, National Institute of Standards and Technology, Gaithersburg, MD 20899, USA. [3]Van't Hoff Institute for Molecular Sciences, University of Amsterdam, Science Park 904, 1098 XH Amsterdam, Netherlands. [4]The Bragg Institute, Australian Nuclear Science and Technology Organisation, PMB1, Menai, NSW, Australia. [5]Materials Sciences Division, Lawrence Berkeley National Laboratory, Berkeley, CA 94720, USA.

*To whom correspondence should be addressed. E-mail: jrlong@berkeley.edu.

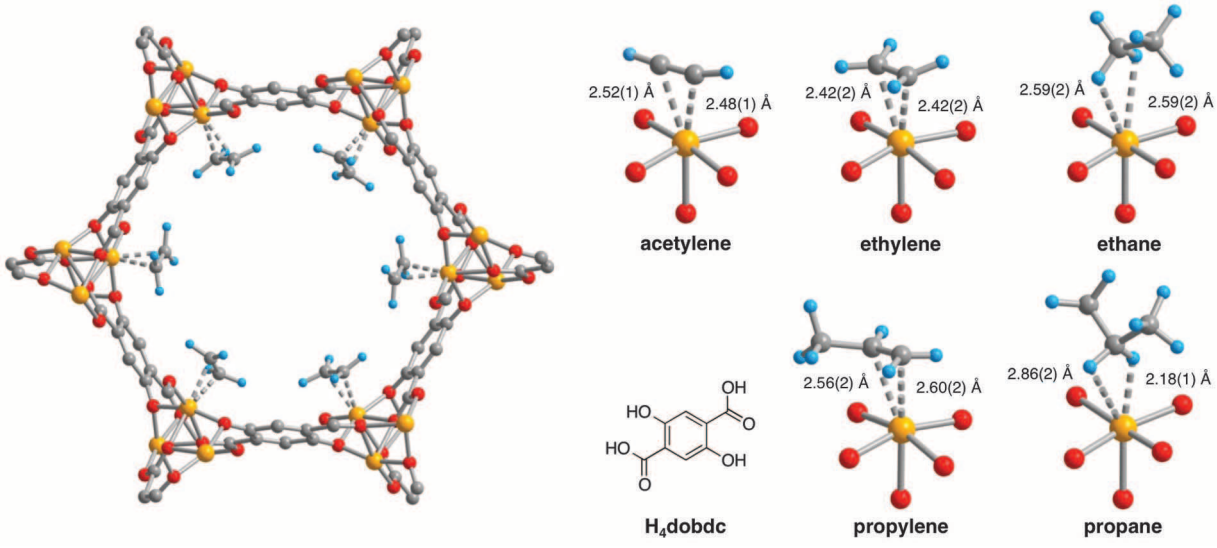

Fig. 1. (**Left**) A portion of the solid-state structure of $Fe_2(dobdc)\cdot 2C_2D_4$ as determined by analysis of neutron powder diffraction data; orange, red, gray, and blue spheres represent Fe, O, C, and D atoms, respectively. The view is along the [001] direction and shows an ethylene molecule bound to the open coordination site at each iron(II) center. (**Right**) H_4(dobdc) ligand and the first coordination spheres for the iron centers in the solid-state structures obtained upon dosing Fe_2(dobdc) with acetylene, ethylene, ethane, propylene, and propane. For propane in Fe_2(dobdc), the adsorbed hydrocarbon molecule has orientational disorder with respect to the open metal center. Of several refined models, the single molecule with large displacement parameters is the most reasonable.

stantially longer than the separations of 2.020(5) to 2.078(4) Å observed for the diamagnetic complex $[Fe(C_2H_4)_4]^{2-}$, one of the very few iron(II)-olefin species to be structurally characterized previously (*19*). The difference suggests that the metal centers within Fe_2(dobdc) maintain a high-spin electron configuration when binding these gases, consistent with weaker interactions that can be reversed with little energy penalty. The interactions of both ethane and propane with the metal cations in Fe_2(dobdc) are even weaker, as evidenced by the elongated Fe-C distance of ~3 Å. This is in good agreement with the Mg-C distance reported for methane adsorption in Mg_2(dobdc), a system in which the metal-adsorbate interactions are also a result of ion-induced dipole interactions between coordinatively unsaturated metal cations and a hydrocarbon (*20*).

Variable-temperature magnetic susceptibility measurements were performed to probe the electronic state of the iron centers in Fe_2(dobdc) upon gas binding. As shown in Fig. 3, Fe_2(dobdc) itself displays a $\chi_M T$ value of 6.40 cm^3K/mol at 300 K, which gradually rises as the temperature decreases before turning over and dropping sharply below 28 K. The behavior is consistent with the presence of high-spin (S = 2) iron(II) centers exhibiting weak [J = 4.1(1) cm^{-1}] ferromagnetic coupling along the oxo-bridged chains running parallel to the c axis, together with still weaker antiferromagnetic coupling between chains. Under a pressure of 1 bar of methane, ethane, ethylene, acetylene, propane, or propylene, the high-spin electron configuration of the iron(II) centers is maintained, but the nature of the magnetic exchange along the chains is altered to varying extents. Weakly interacting adsorbates, such as methane, ethane, and propane, slightly diminish the strength of the ferromagnetic exchange, whereas the more strongly interacting propylene, ethylene, and acetylene perturb the electron density at the iron(II) centers sufficiently to reverse the nature of the intrachain coupling from ferromagnetic to antiferromagnetic. Moreover, the J values resulting from the fits to the data provide a qualitative measure of the adsorbate binding energy, suggesting that the strength of the iron(II)-hydrocarbon interactions increase along the series methane < ethane < propane < propylene < acetylene < ethylene.

The strength of hydrocarbon binding within Fe_2(dobdc) was determined quantitatively through analysis of the gas adsorption data. The data for acetylene, ethylene, ethane, propane, and propylene, expressed in terms of absolute loadings, were fitted with the dual-Langmuir-Freundlich isotherm model, whereas methane adsorption data were fitted with a single-site Langmuir model (*21*). Isosteric heats of adsorption were then calculated from the fits to compare the binding enthalpies of these gases under various loadings (fig. S3). Heats of adsorption for acetylene (–47 kJ/mol), ethylene (–45 kJ/mol), and propylene (–44 kJ/mol) show a significant reduction as the loading approaches the value corresponding to one gas molecule per iron(II) center, again consistent with the exposed metal cations presenting the strongest adsorption sites in the material. Propane (–33 kJ/mol), ethane (–25 kJ/mol), and methane (–20 kJ/mol) adsorption enthalpies are all considerably lower in magnitude, with the trend reflecting the decreasing polarizabilities of these molecules from propane to ethane to methane.

Adsorption selectivities were calculated using ideal adsorbed solution theory (IAST) (*22*), using the fitted isotherms of the experimental isotherm data for relevant gas mixtures in Fe_2(dobdc) and a number of other porous materials for which analogous gas uptake properties have been reported (fig. S4). For an equimolar mixture of ethylene and ethane at 318 K, the adsorption selectivities obtained for Fe_2(dobdc) of 13 to 18 are significantly greater than those calculated for either zeolite NaX or the isostructural metal-organic framework Mg_2(dobdc), which display selectivities of 9 to 14 and 4 to 7, respectively (*17*, *23*). The latter result is consistent with the softer character of Fe^{2+} relative to Mg^{2+}, leading to a stronger interaction with the π electron cloud of the olefin. Similarly, in comparing the performance of Fe_2(dobdc) with other porous materials for the separation of a propane/propylene mixture (selectivity = 13 to 15), it is rivaled in selectivity only by zeolite ITQ-12, which displays adsorption selectivity of 15 while the other materials display selectivities from 3 to 9 (*24*). However,

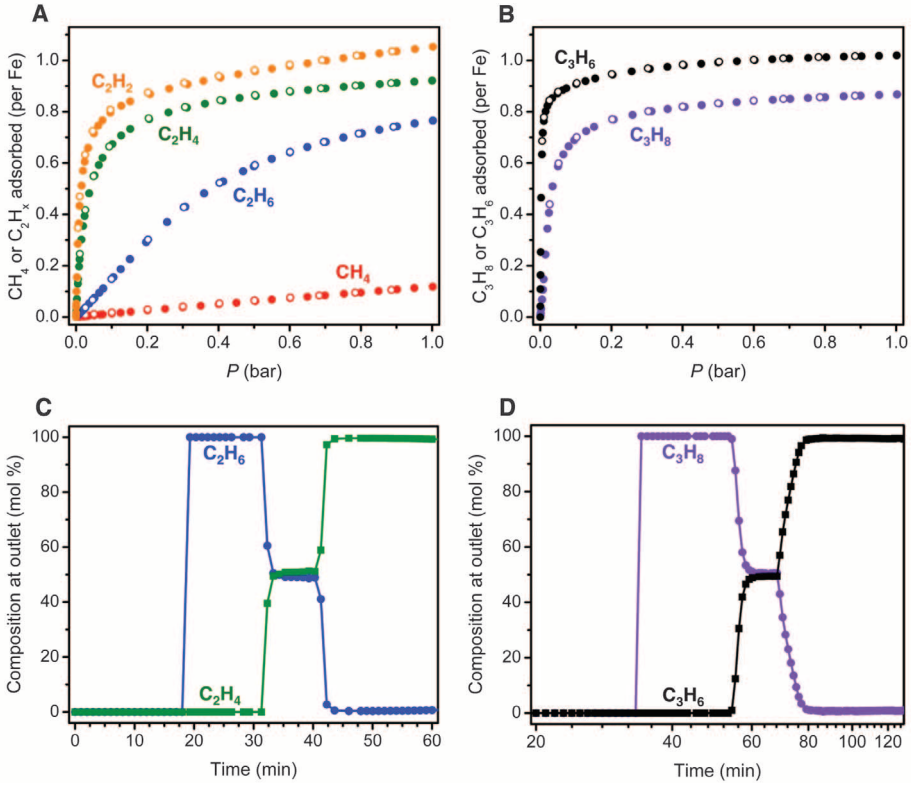

Fig. 2. (**A** and **B**) Gas adsorption isotherms for (A) methane, ethane, ethylene, and acetylene and (B) propane and propylene in Fe_2(dobdc) at 318 K. Filled and open circles represent adsorption and desorption data, respectively. The adsorption capacities at 1 bar correspond to 0.77, 5.00, 6.02, 6.89, 5.67, and 6.66 mmol/g, respectively. (**C** and **D**) Experimental breakthrough curves for the adsorption of equimolar (C) ethane/ethylene and (D) propane/propylene mixtures flowing through a 1.5-mL bed of Fe_2(dobdc) at 318 K with a total gas flow of 2 mL/minute at atmospheric pressure. After breakthrough of the olefin and return to an equimolar mixture composition, a nitrogen purge was applied, leading to desorption of the olefin. In an actual separation scenario, desorption would instead be carried out by applying a vacuum and/or raising the temperature.

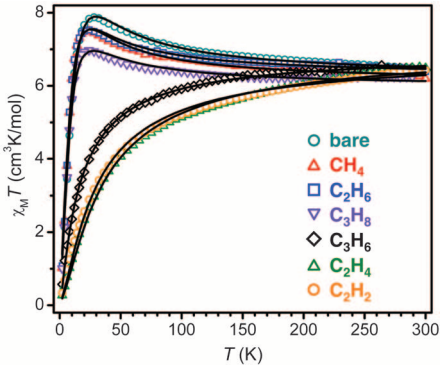

Fig. 3. Variable-temperature magnetic susceptibility data in an applied field of 1 kOe for samples of Fe_2(dobdc) in a vacuum (bare) and under 1 bar of the indicated hydrocarbon. Black lines represent fits to a Hamiltonian derived using the Fisher model for a one-dimensional chain of exchange-coupled S = 2 ions, with an additional term to account for interchain coupling. Full details of the model and fit parameters can be found in table S17 and accompanying text.

the selectivities of ITQ-12 for this mixture were calculated from data collected at 303 K, and it is expected that the selectivity of this material will be lower at higher temperatures. Adsorption selectivities were also calculated using IAST for Fe_2(dobdc) in an equimolar four-component mixture of methane, ethane, ethylene, and acetylene at 318 K, as relating to the purification of natural gas. For an adsorption-based process operating at 1 bar, the calculated acetylene/methane, ethylene/methane, and ethane/methane selectivities are 700, 300, and 20, respectively. These values are much higher than those recently reported (13.8, 11.1, and 16.6, respectively) for a zinc-based metal-organic framework, also based on an analogous calculation procedure (*25*).

To evaluate the performance of Fe_2(dobdc) in an actual adsorption-based separation process, breakthrough experiments were performed in which an equimolar ethylene/ethane or propylene/propane mixture was flowed over a packed bed of the solid with a total flow of 2 mL per minute at 318 K (Fig. 2). In a typical experiment, the gas mixture was flowed through 300 to 400 mg of metal-organic framework crystallites packed into a 1.5-mL glass column, and the outlet gas stream was monitored by a gas chromatograph equipped with a flame ionization detector. As expected from the calculated selectivities, in each case, the alkane was first to elute through the bed, whereas the solid adsorbent retained the olefin. For the C_3 hydrocarbons, the outlet gas contained undetectable levels of propylene, resulting in a propane feed that appeared to be 100% pure, within the detection limit of the instrument [~100 parts per million (ppm)]. Upon saturation of the metal centers within the adsorbent, propylene "broke through," and the outlet gas stream then quickly reached equimolar concentrations. By stopping the gas feed and flowing a purge of nitrogen through the bed, the small amount of weakly bound propane remaining in the pores of the framework could be quickly removed, and the iron-bound propylene then desorbed more slowly. Greater than 99% pure propylene was realized during the desorption step of the breakthrough experiment. In a similar manner, breakthrough experiments showed that Fe_2(dobdc) can separate an equimolar mixture of ethylene and ethane into the pure component gases of 99% to 99.5% purity. Differential scanning calorimetry (DSC) experiments (fig. S5) indicate that energies of 0.84 MJ/kg and 1.3 MJ/kg are needed to release propylene and ethylene, respectively, and regenerate the material for subsequent separation steps.

Although breakthrough experiments are quite valuable for evaluating the gas separation capabilities of a material, in practice they can be difficult and time consuming. In order to compare Fe_2(dobdc) with other reported adsorbents for ethylene/ethane and propylene/propane separations, we sought to demonstrate that the breakthrough characteristics could instead be simulated with reasonable accuracy. Assuming that (i) intracrystalline diffusion is negligible through an isothermal adsorption bed in thermodynamic equilibrium, (ii) plug flow proceeds through the bed, and (iii) the binary mixture adsorption equilibrium in the packed bed of crystallites can be calculated using IAST, we were able to solve a set of partial differential equations and calculate breakthrough curves for both ethylene/ethane and propylene/propane mixtures. The resulting transient gas composition profiles (figs. S6 and S7) are in excellent agreement with the experimental results shown in Fig. 1.

Given this validation, we employed analogous simulations to make quantitative comparisons with other materials. From the simulated breakthrough curves, the time interval during which the exit gas compositions have a purity of 99% propane can be determined, together with the amount of 99% pure propane produced in this time interval. The production capacities, expressed as the amount of propane produced per liter of adsorbent, are shown in fig. S8 over a range of pressures for the zeolites ITQ-12 at 303 K and NaX at 318 K, and for the metal-organic frameworks $Cu_3(btc)_2$ (btc^{3-}: 1,3,5-benzenetricarboxylate) at 318 K (*26*), $Cr_3(btc)_2$ (*27*) at 308 K (fig. S9), and Fe-MIL-100 at 303 K (*11*). These results indicate that the propane production capacity of Fe_2(dobdc) at 318 K, which ranges up to 5.8 mol/L at a total pressure of 1.0 bar, is at least 20% higher than that of any of these other materials. A similar method was used to calculate the amount of polymer-grade (99.5%+) propylene that can be produced by these materials, again leading to a higher capacity for Fe_2(dobdc) than for any other material. The compound Mg_2(dobdc) exhibits a lower productivity than Fe_2(dobdc), a result of the lower adsorption selectivity of this material. Although zeolite ITQ-12 displayed a comparable selectivity to Fe_2(dobdc), its capacity limitation, which stems from its low pore volume of 0.134 cm^3/g, results in a propylene productivity that is just 47% of that of the metal-organic framework. For the separation of ethylene/ethane mixtures, the breakthrough simulations indicate an even greater advantage of Fe_2(dobdc) over other adsorbents, with production capacities that are roughly double those of Mg_2(dobdc) and zeolite NaX (fig. S10).

In addition to the separation of binary olefin/paraffin mixtures, there is tremendous current interest in separating ethane, ethylene, and acetylene from methane for the purification of natural gas. Indeed, a number of porous materials (*23*, *28*) are able to selectively separate methane from mixtures including C_2 hydrocarbons (ethane, ethylene, and acetylene). These materials, however, are unable to simultaneously purify the ethane, ethylene, and acetylene being removed from the gas stream. A separation process that uses the same adsorptive material for the separation and purification of all four components of a C_1/C_2 mixture could potentially lead to substantial efficiency and energy savings over current processes. To establish the feasibility of using Fe_2(dobdc) for this task, we carried out breakthrough calculations for such a mixture. Figure 4 presents simulated data on the gas-phase molar concentrations exiting an adsorber packed with Fe_2(dobdc) and subjected to a feed gas consisting of an equimolar mixture of methane, ethane, ethylene, and acetylene at a total pressure of 1 bar and a temperature of 318 K. The breakthrough times reflect the relative adsorption selectivities (acetylene > ethylene > ethane > methane) for the material, and the curves indicate a clean, sharp breakthrough transition for each successive gas.

Based on these results, the diagram at the right in Fig. 4 demonstrates how it might be possible to procure pure methane, ethane, ethylene, and acetylene using three packed beds of Fe_2(dobdc). In this process, a gas mixture is fed into the first bed, and methane—the fraction with the lowest adsorptivity—breaks through first. Pure methane can be collected until the second gas, ethane, breaks through. When the third component of the gas stream, ethylene, is present in the

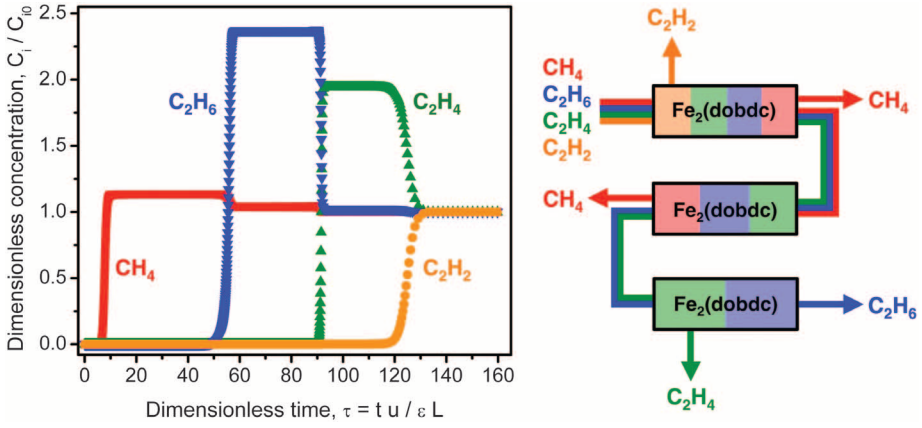

Fig. 4. (**Left**) Calculated methane (red), ethane (blue), ethylene (green), and acetylene (orange) breakthrough curves for an equimolar mixture of the gases at 1 bar flowing through a fixed bed of Fe_2(dobdc) at 318 K. (**Right**) Schematic representation of the separation of a mixture of methane, ethane, ethylene, and acetylene using just three packed beds of Fe_2(dobdc) in a vacuum swing adsorption or temperature swing adsorption process.

eluent, the gas flow is diverted to a second bed, from which additional pure methane is collected during the adsorption step and from which a mixture of ethane and ethylene is subsequently desorbed. This ethane/ethylene mixture is then separated into its pure components using a third adsorbent bed. By halting the feed into the first bed just before the breakthrough of acetylene, pure acetylene can be obtained via desorption.

Ethylene produced in a naphtha cracker contains an impurity of approximately 1% acetylene. However, there are strict limitations to the amount of acetylene that can be tolerated in the feed to an ethylene polymerization reactor. The current technology for this purpose uses absorption with liquid *N*,*N*′-dimethylformamide, but the use of solid adsorbents could potentially provide an energy-efficient alternative. We therefore also investigated the use of Fe_2(dobdc) for removal of acetylene from mixtures with ethylene. Simulated breakthrough characteristics for a feed mixture containing 1 bar of ethylene and 0.01 bar of acetylene at 318 K indicate that final acetylene concentrations on the order of 10 ppm could be realized (fig. S11).

An alternative to the use of pressure swing adsorption for olefin/paraffin separations is to adopt a membrane-based technology. To investigate the potential use of Fe_2(dobdc) membranes for the separation of such mixtures, we applied a simulation methodology previously employed for evaluating idealized Mg_2(dobdc) membranes (*29*, *30*). Here, an equimolar ethylene/ethane or propylene/propane mixture permeates through a contiguous, unsupported layer of Fe_2(dobdc) crystals, all aligned such that the channels of the framework are oriented parallel to the gas flow. Although a membrane of this type would be challenging to prepare, the following results indicate the utility of an unsupported metal-organic framework membrane. The permeation fluxes for the gas components are then related to the gradients in the loadings within the crystals by the Maxwell-Stefan diffusion equations (*29*–*31*). The calculated ethylene/ethane permeation selectivities lie in the range of 13 to 20 for total upstream pressures between 0.1 and 1.0 bar (fig. S12). These values are close to the corresponding adsorption selectivities in Fe_2(dobdc) because the more mobile partner species are slowed down within the one-dimensional channels of the structure. The slowing-down effects are caused by correlations in the molecular hops of the mobile and tardier species in the mixture within the one-dimensional channels of structures such as Fe_2(dobdc) and Mg_2(dobdc) (*31*). Such correlations serve to bring the component diffusivities in the mixture closer to each other.

In other words, strong correlation effects within the one-dimensional channels of Fe_2(dobdc) cause the permeation selectivities to be close to the adsorption selectivities, which, as discussed above, are very high. The calculated permeation selectivities are expected to be reasonably accurate, irrespective of the accuracy of the force field information, because the high degree of correlations within the channels tends to eliminate differences in the component mobilities. Thus, much greater selectivity can be expected for membranes based on Fe_2(dobdc) compared to ZIF-8, for which a permeation selectivity of 2.8 was recently reported (*32*). An important further advantage of the use of Fe_2(dobdc) is that the diffusivities within the 11 Å–wide channels of this material are about two to three orders of magnitude greater than those in ZIF-8, conferring both selectivity and permeability advantages. Similar advantages can be expected for applications of Fe_2(dobdc) in membrane separations of equimolar propylene/propane mixtures, for which permeation selectivities are calculated to lie in the range of 14 to 16 for total upstream pressures between 0.05 and 1.0 bar (fig. S13).

The foregoing results demonstrate the extraordinary prospects for using the metal-organic framework Fe_2(dobdc) as a solid adsorbent in the separation of valuable C_1 to C_3 hydrocarbons through pressure/temperature swing adsorption methods or through membrane-based applications.

References and Notes

1. R. B. Eldridge, *Ind. Eng. Chem. Res.* **32**, 2208 (1993).
2. K. Tanaka, A. Taguchi, J. Hao, H. Kita, K. Okamoto, *J. Membr. Sci.* **121**, 197 (1996).
3. D. J. Safarik, R. B. Eldridge, *Ind. Eng. Chem. Res.* **37**, 2571 (1998).
4. M. Eddaoudi *et al.*, *Science* **295**, 469 (2002).
5. S.-I. Noro, S. Kitagawa, M. Kondo, K. Seki, *Angew. Chem. Int. Ed.* **39**, 2081 (2000).
6. L. J. Murray, M. Dincă, J. R. Long, *Chem. Soc. Rev.* **38**, 1294 (2009).
7. N. L. Rosi *et al.*, *Science* **300**, 1127 (2003).
8. J.-R. Li, R. J. Kuppler, H.-C. Zhou, *Chem. Soc. Rev.* **38**, 1477 (2009).
9. Y.-S. Bae *et al.*, *Chem. Commun. (Camb.)* (35): 4135 (2008).
10. S. Bourrelly *et al.*, *J. Am. Chem. Soc.* **127**, 13519 (2005).
11. J. W. Yoon *et al.*, *Angew. Chem. Int. Ed.* **49**, 5949 (2010).
12. Z. Zhang, S. Xiang, B. Chen, *CrystEngComm* **13**, 5983 (2011).
13. S.-C. Xiang *et al.*, *Nat. Commun.* **2**, 204 (2011).
14. H. Leclerc *et al.*, *Phys. Chem. Chem. Phys.* **13**, 11748 (2011).
15. R. Matsuda *et al.*, *Nature* **436**, 238 (2005).
16. E. D. Bloch *et al.*, *J. Am. Chem. Soc.* **133**, 14814 (2011).
17. Z. Bao *et al.*, *Langmuir* **27**, 13554 (2011).
18. Y.-S. Bae *et al.*, *Angew. Chem. Int. Ed.* **51**, 1857 (2012).
19. A. Fürstner *et al.*, *J. Am. Chem. Soc.* **130**, 8773 (2008).
20. H. Wu, W. Zhou, T. Yildirim, *J. Am. Chem. Soc.* **131**, 4995 (2009).
21. R. Krishna, J. R. Long, *J. Phys. Chem. C* **115**, 12941 (2011).
22. A. L. Myers, J. M. Prausnitz, *AIChE J.* **11**, 121 (1965).
23. S. H. Hyun, R. P. Danner, *J. Chem. Eng. Data* **27**, 196 (1982).
24. J. J. Gutiérrez-Sevillano *et al.*, *J. Phys. Chem. C* **114**, 14907 (2010).
25. M. C. Das *et al.*, *Chemistry* **17**, 7817 (2011).
26. M. G. Plaza *et al.*, *Micropor. Mesopor. Mater.*, published online 14 July 2011.
27. L. J. Murray *et al.*, *J. Am. Chem. Soc.* **132**, 7856 (2010).
28. S. C. Reyes *et al.*, U.S. Patent 12,322,364 (2009).
29. R. Krishna, J. M. van Baten, *J. Membr. Sci.* **377**, 249 (2011).
30. R. Krishna, *J. Phys. Chem. C* **113**, 19756 (2009).
31. R. Krishna, J. M. van Baten, *J. Membr. Sci.* **383**, 289 (2011).
32. H. Bux, C. Chmelik, R. Krishna, J. Caro, *J. Membr. Sci.* **369**, 284 (2011).

Acknowledgments: The data described in this paper are presented in the supporting online material. This research was supported through the Center for Gas Separations Relevant to Clean Energy Technologies, an Energy Frontier Research Center funded by the U.S. Department of Energy, Office of Science, Office of Basic Energy Sciences under award DE-SC0001015. In addition, we thank the National Institute of Standards and Technology National Research Council Postdoctoral Fellowship Research Associate program for support of W.L.Q.; V. K. Peterson and S. N. Maximoff for assistance and helpful discussions; C. J. Kepert for the use of his glovebox to prepare neutron powder diffraction samples; and J. M. van Baten for valuable assistance in the simulation work. Metrical data for the solid-state structures of the acetylene, ethylene, ethane, propylene, and propane adducts of Fe_2(dobdc) are available free of charge from the Cambridge Crystallographic Data Centre under reference numbers CCDC 866357 to 866361. The authors and the University of California, Berkeley have filed a patent on the results presented herein.

Supporting Online Material

www.sciencemag.org/cgi/content/full/335/6076/1606/DC1
Materials and Methods
Figures S1 to S13
Tables S1 to S23
Movies S1 to S11
References (*33*–*45*)

6 December 2011; accepted 16 February 2012
10.1126/science.1217544

$^{238}U/^{235}U$ Systematics in Terrestrial Uranium-Bearing Minerals

Joe Hiess,[1]* Daniel J. Condon,[1] Noah McLean,[2] Stephen R. Noble[1]

The present-day $^{238}U/^{235}U$ ratio has fundamental implications for uranium-lead geochronology and cosmochronology. A value of 137.88 has previously been considered invariant and has been used without uncertainty to calculate terrestrial mineral ages. We report high-precision $^{238}U/^{235}U$ measurements for a suite of uranium-bearing minerals from 58 samples representing a diverse range of lithologies. This data set exhibits a range in $^{238}U/^{235}U$ values of >5 per mil, with no clear relation to any petrogenetic, secular, or regional trends. Variation between comagmatic minerals suggests that $^{238}U/^{235}U$ fractionation processes operate at magmatic temperatures. A mean $^{238}U/^{235}U$ value of 137.818 ± 0.045 (2σ) in zircon samples reflects the average uranium isotopic composition and variability of terrestrial zircon. This distribution is broadly representative of the average crustal and "bulk Earth" $^{238}U/^{235}U$ composition.

The uranium-lead (U-Pb) system is widely used as an isotopic chronometer for geological and meteoritic materials that are less than 1 million to greater than 4.5 billion years old. This system is particularly useful because it has two long-lived isotopes, ^{238}U and ^{235}U,

Supplementary Materials for

Hydrocarbon Separations in a Metal-Organic Framework with Open Iron(II) Coordination Sites

Eric D. Bloch, Wendy L. Queen, Rajamani Krishna, Joseph M. Zadrozny, Craig M. Brown, Jeffrey R. Long*

*To whom correspondence should be addressed. E-mail: jrlong@berkeley.edu

Published 30 March 2012, *Science* **335**, 1606 (2012)
DOI: 10.1126/science.1217544

This PDF file includes:

Other Supporting Online Material for this manuscript includes the following:
(available at www.sciencemag.org/cgi/content/full/335/6076/1606/DC1)

Table of Contents

Materials and Methods

1.1 Synthesis and Low-Pressure Gas Adsorption Measurements

The synthesis of Fe_2(dobdc) was performed as previously reported.(*16*) For all gas adsorption measurements 200-225 mg of Fe_2(dobdc)·4MeOH was transferred to a pre-weighed glass sample tube under an atmosphere of nitrogen and capped with a Transeal. Samples were then transferred to Micromeritics ASAP 2020 gas adsorption analyzer and heated at a rate of 0.1 K/min from room temperature to a final temperature of 433 K. Samples were considered activated when the outgas rate at 433 K was less than 2 μbar/min. Evacuated tubes containing degassed samples were then transferred to a balance and weighed to determine the mass of sample, typically 150-175 mg. The tube was transferred to the analysis port of the instrument where the outgas rate was again determined to be less than 2 μbar/min at 433 K. All measurements were performed using a recirculating dewar connected to an isothermal bath. For acetylene adorption 99.5 % purity gas was used while 99.99% or higher purity gases were used for methane, ethane, ethylene, propane, and propylene.

1.2 Differential Scanning Calorimetry

Thermal analysis was performed on a TA Instruments Q200 differential scanning calorimeter equipped with a refrigerated cooling system (RCS40). Through the sample cell 100 % ethylene, propylene, or acetylene were flowed over hermetically sealed T-Zero aluminum pans that had been pierced under an argon atmosphere. An empty T-Zero pan provided the reference for thermal analysis. Integrated heats were calculated with TA Instruments Universal Analysis software suite.

1.3 Magnetic Measurements and Susceptibility Fitting Details

Magnetic data were collected using a Quantum Design MPMS-XL SQUID magnetometer. Measurements on Fe_2(dobdc) were obtained with finely ground microcrystalline powders restrained with a plug of glass wool within a sealed quartz tube. No effects of crystallite torqueing were observed. Preparation of the gas-loaded samples was accomplished by attaching a sample of pure Fe_2(dobdc), loaded in a quartz tube, to a Micromeritics ASAP 2020 Surface Area and Porosity Analyzer. The pressure of the atmosphere of the sample tube was then adjusted to 1 bar of the specific hydrocarbon gas, the tube cooled in liquid N_2, and sealed with a hydrogen flame. Dc susceptibility measurements were collected in the temperature range 2-300 K under a dc field of 1000 Oe. To avoid possible effects due to flash-freezing of the samples and the sealed gasses, all samples were cooled slowly from 300 to 2 K during the course of the measurement. Dc magnetic susceptibility data were corrected for diamagnetic contributions from the sample holder and glass wool, as well as for the core diamagnetism of each sample (estimated using Pascal's constants).(*33*)

The temperature dependence of the magnetic susceptibility of the framework was modeled as a chain of Heisenberg spins interacting (*34*) with three other chains in the molecular field approximation.(*35*) This is represented via the following Hamiltonian:

$$\hat{H} = -2J \sum_i \boldsymbol{S}_{\mathrm{Fe}(i)} \boldsymbol{S}_{\mathrm{Fe}(i+1)} - M\boldsymbol{B} \sum_i \boldsymbol{S}_{\mathrm{Fe}(i)} - zJ' \langle S_{\mathrm{Fe}} \rangle \mathbf{S}_{\mathrm{Fe}}$$

Here, J represents the intrachain Fe-Fe superexchange coupling constant, $\mathbf{S}_{\mathrm{Fe}(i)}$ and $\boldsymbol{S}_{\mathrm{Fe}(i+1)}$ the spin operators for the Fe ions of the chain, $M\boldsymbol{S}_{\mathrm{Fe}(i)}$ corresponds to the magnetic moment of the Fe(i) spin, $\boldsymbol{B}$ is the applied field, z the number of interacting nearest-

neighbors, J' the interchain coupling constant, and $\langle S_{Fe} \rangle$ the mean value of the S_z component of the S_{Fe} operator. In section of the crystal structures reveals that each Fe-chain has 3 other chains to which it is connected. Therefore, z has been set to 3 for all fits. The equation used to fit the variable temperature magnetic susceptibility data, derived from the Hamiltonian above, is:

$$\chi_{Fit} = \frac{3kg_{iso}^2 F(J,T)}{8\left(kT - 3J'F(J,T)\right)}$$

where:

$$F(J,T) = 2\frac{(1+u)}{(1-u)}$$

where:

$$u = \frac{\cosh(6J/kT)}{\sinh(6J/kT)} - \frac{kT}{6J}$$

Here, k is the Boltzmann constant, g_{iso} is the isotropic Landé g-factor, J is the intra-chain exchange coupling constant, and T is the temperature. The following table presents the best fit results of g, J and J' for the activated framework and the framework under 1 bar atmospheres of the studied hydrocarbons. J' was allowed to vary for the fits, but was constrained to stay within $0 > J' > -1.5$ cm^{-1}.

1.4 Neutron Powder Diffraction Data

Neutron powder diffraction measurements of the bare and hydrocarbon-loaded Fe_2(dobdc) were performed on the Echidna instrument (*36*) located at the Bragg Institute of the Australian Nuclear Science and Technology Organisation (ANSTO). An activated sample weighing 1.079 g was transferred to a vanadium cell in an Ar-filled glovebox. The cell was equipped with heaters for the gas line and valve to allow condensable gases to be loaded in the sample when mounted in the closed cycle refrigerator. The high-resolution diffractometer was configured with a Ge(311) monochromator using a take-off angle of 140° with no collimation at the monochromator and fixed tertiary 5' collimation, resulting in a wavelength of 2.4406 Å. Diffraction data were collected at ≈9 K for the evacuated framework and with specified loadings between 0.5 and 1.0 deuterated hydrocarbons per Fe^{2+}. The hydrocarbons were loaded in to the sample with the cryostat and sample initially at 300 K. The material was allowed to reach an equilibrium pressure and then slowly cooled to ensure total adsorption as determined by a zero pressure reading on a pressure gauge above the freezing point of the gas. Between adsorption of different hydrocarbons the sample was heated to 300 K *in-situ* and evacuated with a further *ex-situ* heating/evacuation at 375 K for a period of at least one hour and a stable pressure reading of ≈1e-6 mbar. Data were integrated over a central region of pixels (45 to 73 out of 128) for the position sensitive detectors.

Neutron powder diffraction data were analyzed using the Rietveld method as implemented in EXPGUI/GSAS.(*37,38*) The activated Fe_2(dobdc) model was refined with all structural and peak profile parameters free to vary. Fourier difference methods were employed to locate the adsorbed hydrocarbon molecules for subsequently collected data, which were then modeled using individual atoms whose fractional occupancy and

isotropic atomic displacement parameter (ADP) were constrained to be the same within each molecule. Further, structural features including bond angles and distances of the adsorbed molecules were initially restrained to values expected for the ideal hydrocarbon. With the exception of propane, once a good structural model was obtained the restrained bond distances and angles were allowed to vary. For the propane adsorbed Fe_2(dobdc), the hydrocarbons appear to have some orientational disorder with respect to the open metal center. This could be the result of intermolecular interactions between neighboring adsorbed molecules at loadings above 0.5 per Fe^{2+}, as this molecule now occupies a significant portion of the pore volume. While the model was refined with multiple orientations of the hydrocarbon, no significant improvements in the structural refinement were possible, and we opted to refine the model with anisotropic displacement parameters to capture the distribution of atomic positions.

Supplementary Text

2. Dual-Langmuir-Freundlich fits of pure component isotherms.

2.1 Adsorption in Fe_2(dobdc)

The measured experimental data on pure component isotherms for methane, acetylene, ethylene, ethane, propane, and propylene in Fe_2(dobdc) were first converted to absolute loading using the Peng-Robinson equation of state for estimation of the fluid densities. The pore volume of Fe_2(dobdc) used for this purpose was 0.626 cm^3/g.

The pure component isotherm data for acetylene, ethylene, ethane, propane, and propylene in Fe_2(dobdc), expressed in terms of absolute loadings, were fitted with the dual-Langmuir-Freundlich isotherm model

$$q_i = q_{i,A,sat}\frac{b_{i,A}p_i^{\nu_{i,A}}}{1+b_{i,A}p_i^{\nu_{i,A}}} + q_{i,B,sat}\frac{b_{i,B}p_i^{\nu_{i,B}}}{1+b_{i,B}p_i^{\nu_{i,B}}} \quad (1)$$

The saturation capacities $q_{i,sat}$, Langmuir-Freundlich parameters b_i, along with the exponents ν_i, for the two sites, A, and B, are provided in Tables S1-S5.

Figure S1 compares the experimental data with the dual-site Langmuir-Freundlich fits.

For adsorption of methane in Fe_2(dobdc) a single-site Langmuir model was sufficiently good for fitting purposes; the Langmuir parameters are specified in Table 6. Figure S1 shows the pure component isotherm data for methane in Fe_2(dobdc) at 318 K, 333 K, and 353 K, in terms of absolute molar loadings. The continuous solid lines are the single-site Langmuir fits using the parameters specified in Table 6.

2.2 Adsorption in Mg_2(dobdc)

For comparison of the ethylene/ethane and propylene/propane separation characteristics of Fe_2(dobdc) with Mg_2(dobdc) the experimental data on pure component isotherms at 318 K reported by Bao et al. were used. The dual-Langmuir-Freundlich fit parameters provided in Table 1 of Bao et al. could be used directly, with the need for re-fitting.(*17*)

2.3 Adsorption in zeolite NaX

For comparison of the ethylene/ethane and propylene/propane separation characteristics of Fe_2(dobdc) with NaX zeolite, experimental isotherm data available in the literature were used.

For ethylene and ethane adsorption, the experimental data of Hyun and Danner, (*22*)determined at temperatures T = 298 K, and 323 K were fitted with equation (1). The dual-site Langmuir-Freundlich parameters are provided in Table S7, and S8.

For propylene and propane adsorption in NaX zeolite, the data provided in Table 4 of the paper by Lamia et al. were used;(*39*) the parameter fits for T = 318 K are specified in Table S9.

2.4 Adsorption in FeMIL-100

For comparison of the propylene/propane separation characteristics of Fe_2(dobdc) with FeMIL-100, experimental isotherm data at 303 K available in the paper by Yoon et al. (*11*) were fitted with a single-site Langmuir-Freundlich isotherm model. It is noteworthy that the pure component experimental data are available up to pressures of 7 kPa. Extrapolation to 100 kPa is therefore not justified. The calculations presented here are only up to a total pressure of 20 kPa. The single-site Langmuir-Freundlich parameters for propylene and propane isotherms in FeMIL-100 at 303 K are given in Table S10.

2.5 Adsorption in ITQ-12

For comparison of the propylene/propane separation characteristics of Fe_2(dobdc) with ITQ-12, experimental isotherm data at 303 K available in the paper by Gutiérrez-Sevillano et al. (*23*) were fitted with a single-site Langmuir-Freundlich isotherm model. The single-site Langmuir-Freundlich parameters for propylene and propane isotherms at 303 K are given in Table S11.

2.6 Adsorption in $Cu_3(btc)_2$

For comparison of the propylene/propane separation characteristics of Fe_2(dobdc) with $Cu_3(btc)_2$, the dual-site Langmuir-Freundlich isotherm model parameters at 318 K, obtained from the parameters supplied in Table 3 of the paper by Plaza et al.,(*25*) were used. The parameters are specified in Table S12.

2.7 Adsorption in $Cr_3(btc)_2$

For comparison of the propylene/propane separation characteristics of with $Cr_3(btc)_2$, unpublished experimental data at 308 K, measured in our group were used. The experimental data are shown in Figure S2, along with the dual-site Langmuir-Freundlich fits using the parameters for propylene and propane isotherms in $Cr_3(btc)_2$ at 308 K specified in Table S13.

3. Isosteric Heat of Adsorption

The isosteric heat of adsorption, Q_{st}, defined as

$$Q_{st} = RT^2 \left(\frac{\partial \ln p}{\partial T} \right)_q \tag{2}$$

were determined using the pure component isotherm fits. Figure S3 presents data on the loading dependence of Q_{st} for adsorption of methane, acetylene, ethylene, ethane,

propane, and propylene in Fe_2(dobdc). The heat of adsorption of the alkenes is significantly higher than that of the corresponding alkane at loadings lower than 5 mol/kg. The Q_{st} for alkenes show a significant reduction as the loadings approach that corresponding to 1 molecule of alkene per Fe atom in the Fe_2(dobdc) framework; this corresponds to a molar loading of 6.5 mol/kg. A similar loading dependence is observed for CO_2 adsorption in the Mg_2(dobdc), and the discussions of Mason et al. are also applicable here.(*40*)

4. IAST Calculations of Adsorption Selectivities

Using the pure component isotherm fits, the adsorption selectivities defined by

$$S_{ads} = \frac{q_1/q_2}{p_1/p_2} \quad (3)$$

can be determined using the Ideal Adsorbed Solution Theory (IAST) of Myers and Prausnitz.(*22*)

Figure S4 shows the IAST calculations of the adsorption selectivity, S_{ads}, for equimolar ethylene/ethane mixtures. It is also to be noted that the NaX selectivity at 298 K is higher than at 323 K. This is the trend that is valid for any porous material; the S_{ads} decreases with increasing T. The selectivities with Fe_2(dobdc) are higher than for both Mg_2(dobdcc) and NaX zeolite over the entire range of pressures.

Figure S4 shows the IAST calculations of the adsorption selectivity, S_{ads}, for equimolar propylene/propane mixtures in a variety of porous materials. In comparing the separation performance of Fe_2(dobdc) with other porous materials. At total gas pressures greater than 50 kPa, the hierarchy of adsorption selectivities is ITQ-12 (at 300 K) > Fe_2(dobdc) (at 318 K) > Mg_2(dobdc) (at 318 K) ≈ NaX (at 318 K) > $Cu_3(btc)_2$ (at 318 K) > $Cr_3(btc)_2$ (at 308 K) > FeMIL-100 (at 303 K). We shall see later that the production capacities of propylene and propane in adsorber are not dictated solely by the adsorptions selectivities.

Figure S4 also shows the IAST calculations of the adsorption selectivity, S_{ads}, for equimolar acetylene/ethylene mixtures using Fe_2(dobdc).

5. Simulations of Breakthrough of Propylene/Propane Mixtures in a Packed Bed Adsorber

Breakthrough experiments were carried out in a 4 mm tube packed with Fe_2(dobdc) crystallites. The sample material of 375 mg was packed within 120 mm of the tube length, i.e. L = 0.12 m. The volume of the adsorber tube is 1.508 mL. The framework density of Fe_2(dobdc) is 1126 kg/m^3. The 375 mg sample occupies a volume of 0.333 mL. Therefore the porosity of the adsorber bed is $\varepsilon = 1 - 0.333/1.508 = 0.779$. The breakthrough experiments with ethylene/ethane, and propylene/propane were performed at a temperature of 318 K and atmospheric pressure conditions. The flow rates of the entering alkane/alkene was maintained at 1 mL/min each. The superficial gas velocity, u, at the entrance of the tube corresponds to 0.00265 m/s. The *characteristic* contact time between the gas and the Fe_2(dobdc) crystallites, $\varepsilon L/u$ = 35.25 s. Typical breakthrough

characteristics for propylene/propane mixture are shown in Figure S5. The *x*-axis is a *dimensionless* time, τ, obtained by dividing the actual time, *t*, by the contact time between the gas and the crystallites, $\varepsilon L/u$.

Our first task is to demonstrate that the breakthrough characteristics can be *simulated* with reasonable accuracy with the following set of assumptions.

(1) Isothermal conditions can be assumed to prevail throughout the bed.
(2) Thermodynamic equilibrium can be assumed to prevail at any location within the packed adsorber bed.
(3) The binary mixture adsorption equilibrium in the packed bed of Fe_2(dobdc) crystallites can be calculated using the IAST.
(4) Plug flow of gas mixture along the bed.
(5) Intra-crystalline diffusion can be considered to be negligible. This is a reasonable assumption for the 1 nm channels of Fe_2(dobdc) crystallites.

With the above set of assumptions, the breakthrough characteristics require the solution of a set of partial differential equations

$$\frac{1}{RT}\varepsilon\frac{\partial p_i}{\partial t} = -\frac{1}{RT}\frac{\partial\left(up_i\right)}{\partial z} - \left(1-\varepsilon\right)\rho\frac{\partial q_i}{\partial t}; \quad i = 1,2,...n \tag{4}$$

using the numerical procedure described in the work of Krishna and Long.(*21*) For T = 318 K, and partial pressures of propylene and propane at the gas inlet maintained at p_{10} = p_{20} = 50 kPa, the molar concentrations of the gas phase exiting the adsorber are shown in Figure S5. The corresponding gas compositions expressed in mol% are also shown in Figure S5.

Having established the potency of breakthrough simulations in reproducing the separation characteristics of the alkane/alkene adsorber, we proceed further in using such simulations for quantitative evaluation of the separation characteristics of Fe_2(dobdc), along with other materials. From the breakthrough compositions the (dimensionless) time interval $\Delta\tau_{ads}$, during which the exit gas compositions has a purity of 99% propane, can be determined. This purity specification has been chosen arbitrarily. From a mass balance on the adsorber, the amount of 99% pure propane produced in this time interval can be determined. The production capacities expressed as the amount of propane produced, with 99%+ purity, per L of Fe_2(dobdc), for a range of total pressures at the inlet to the adsorber are shown in Figure S6 along with the the propane production capacities of ITQ-12 (at 300 K), NaX (at 318 K), $Cu_3(btc)_2$ (at 318 K), $Cr_3(btc)_2$ (at 308 K), and FeMIL-100 (at 303 K). It is to be noted that for FeMIL-100, the pressures range to 20 kPa because the isotherm fits are only valid for this range. For a fair comparison of separation characteristics, the volume of adsorbent used in the tube is held constant at the value corresponding to that used for Fe_2(dobdc); this corresponds to 0.333 mL in the 4 mm tube of packed length 120 mm. The masses of the adsorbent materials are determined by the framework densities: ITQ-12: 1792 kg m^{-3}; NaX: 1421 kg m^{-3}, $Cu_3(btc)_2$: 878 kg m^{-3}, $Cr_3(btc)_2$: 828kg m^{-3}, and FeMIL-100: 593 kg m^{-3} .

After the adsorption phase is complete, the contents of the bed are desorbed. The desorption can be done by purging the contents of the bed with inert, non-adsorbing, gas. The transient desorption characteristics of the bed, for which the bed constants correspond to the end of the adsorption cycle in Figure S5. From the desorption characteristics, we note that there is a time interval $\Delta\tau_{des}$, during which the exit gas

compositions has a purity of 99.5% propylene. This purity specification corresponds to that of polymer-grade propylene. From a mass balance on the adsorber, the production capacity of polymer-grade propylene can be determined. The production capacities expressed as the amount of propylene produced, with 99.5%+ purity, per L of Fe_2(dobdc), for a range of total pressures at the inlet to the adsorber are shown in Figure S5 for various materials. From this plot we note that the polymer-grade propylene production capacity of Fe_2(dobdc) is higher than that of any other material. Mg_2(dobdc) has a slightly lower productivity than Fe_2(dobdc), and the reason for this can be traced to a lower adsorption selectivity.

The severe capacity limitation of ITQ-12 is the reason for its remarkably lower productivity, despite have the highest adsorption selectivity, S_{ads}. The capacity limitation of ITQ-12 is due to its extremely low pore volume, 0.134 cm^3/g.

Video animations of both the transient adsorption/desorption cycles for propylene/propane mixtures in Fe_2(dobdc) and NaX zeolite have been provided as supplementary material accompanying this publication.

6. Simulations of Breakthrough of Ethylene/Ethane Mixtures in a Packed Bed Adsorber

For separation of ethylene/ethane mixtures using Fe_2(dobdc) the simulations of the breakthrough characteristics were of the adsorption and desorption cycles are shown in figure S7. From these transient characteristics, the production capacities for ethane (arbitrarily chosen to be 99% purity), and ethylene (polymer-grade with 99.5%+ purity) can be determined from a mass balance over the adsorber for the time intervals $\Delta\tau_{ads}$, and $\Delta\tau_{des}$ indicated in Figure S7. The production capacities expressed as the amount of ethane, and ethylene, per L of adsorbent material, for a range of total pressures at the inlet to the adsorber are shown in Figure S8. We note that the production capacities with Fe_2(dobdc) are nearly double that of both Mg_2(dobdc) and NaX zeolite.

Video animations of both the transient adsorption/desorption cycles for ethylene/ethane mixtures using Fe_2(dobdc) and NaX zeolite have been provided as supplementary material accompanying this publication.

7. Investigating the Potential of Fe_2(dobdc) Membranes for Alkane/Alkene Separations

For a range of upstream pressures, the permeation selectivity, S_{perm} defined by

$$S_{perm} = \frac{N_1/N_2}{p_{10}/p_{20}} \tag{5}$$

were determined by numerical solution of the set of Maxwell-Stefan diffusion equations, as described in previous works.(*21,28*) The adsorption equilibrium is determined by use of the IAST, using the same procedure adopted in the breakthrough calculations. All calculations were performed for isothermal conditions at 318 K. The pure component isotherm data fits provided in Tables 1-5 The Maxwell-Stefan diffusivities, of the pure components were determined by performing Molecular Dynamics (MD) simulations,

using the methodology described in previous works.(*28-30*) The force field information is provided in Table S14.

The MD simulated data are presented in Figure S11. The diffusivities of ethylene and ethane are within 20% of each other; this is in line with the experimental data of Bao et al. for propane and propylene in Mg_2(dobdc). Also in line with the experimental data of Bao et al. is the observation that the diffusivities of propylene and propane lie close together. An important consideration in mixture permeation is the proper modeling of correlation effects. Such correlation effects have the effect of slowing down the more mobile species. Such correlation effects will have the effect of washing out, even further, the already small differences in the diffusivities in the ethane/ethane and propylene/propane mixtures. For quantification of the correlation effects, the self-exchange coefficients were determined from MD simulations. The MD simulated data on the degree of correlations were fitted with the parameter values presented in Table S15.

8. Notation

b_i	dual-Langmuir-Freundlich constant for species *i*, $Pa^{-\nu_i}$
$Đ_i$	Maxwell-Stefan diffusivity, $m^2\ s^{-1}$
$Đ_{ii}$	self exchange coefficient, $m^2\ s^{-1}$
L	length of packed bed adsorber, m
N_i	molar flux of species *i* defined in terms of the membrane area, mol $m^{-2}\ s^{-1}$
p_i	bulk gas pressure of species *i*, Pa
q_i	component molar loading of species *i*, mol kg^{-1}
$q_{i,sat}$	saturation loading of species *i*, mol kg^{-1}
S_{perm}	permeation selectivity, dimensionless
t	time, s
T	temperature, K
u	superficial gas velocity, m s^{-1}

Greek letters

□	voidage of packed bed, dimensionless
□$_i$	exponent in the dual-Langmuir-Freundlich isotherm, dimensionless
□	dimensionless time

Subscripts

i	referring to component *i*
A	referring to site A
B	referring to site B

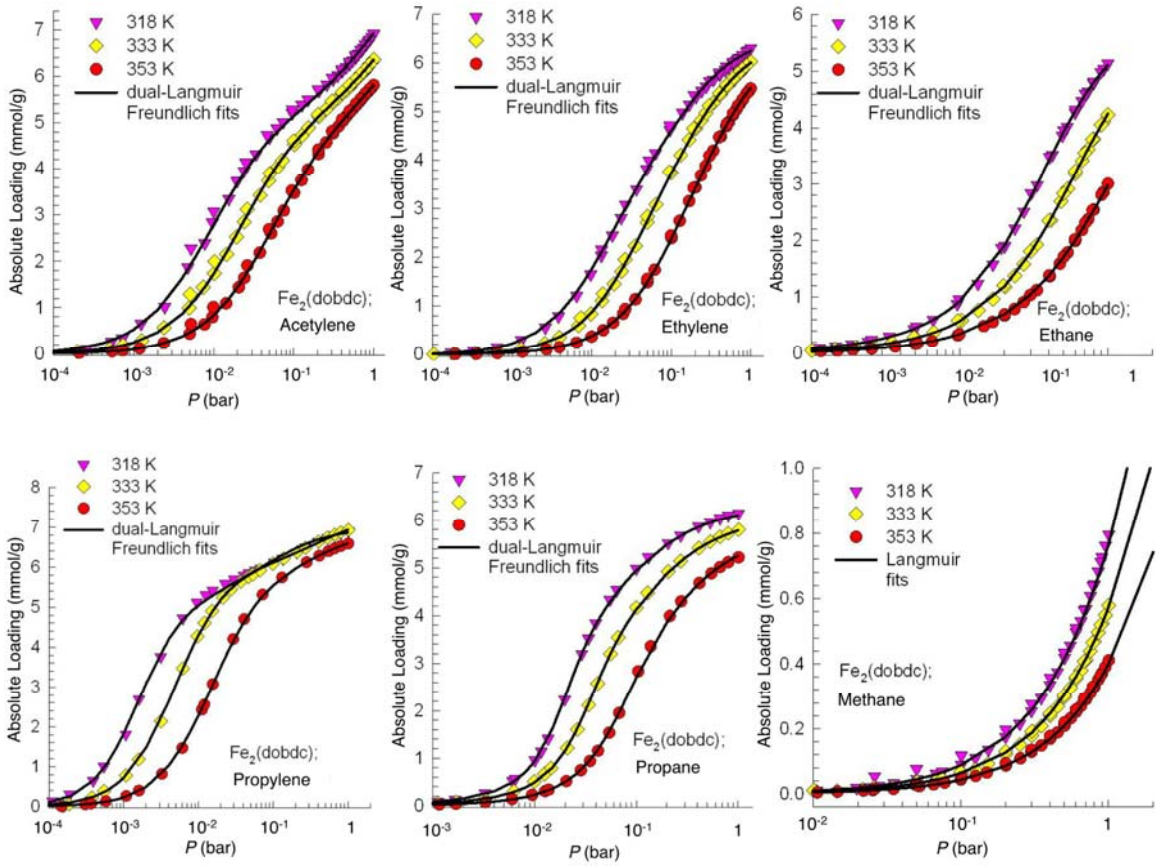

Fig. S1.

The pure component isotherm data for methane, ethane, ethylene, propane, propylene, and acetylene in $Fe_2(dobdc)$ at 318 K, 333 K, and 353 K, in terms of absolute molar loadings. The continuous solid lines are fits using the parameters specified in Tables S1-S6.

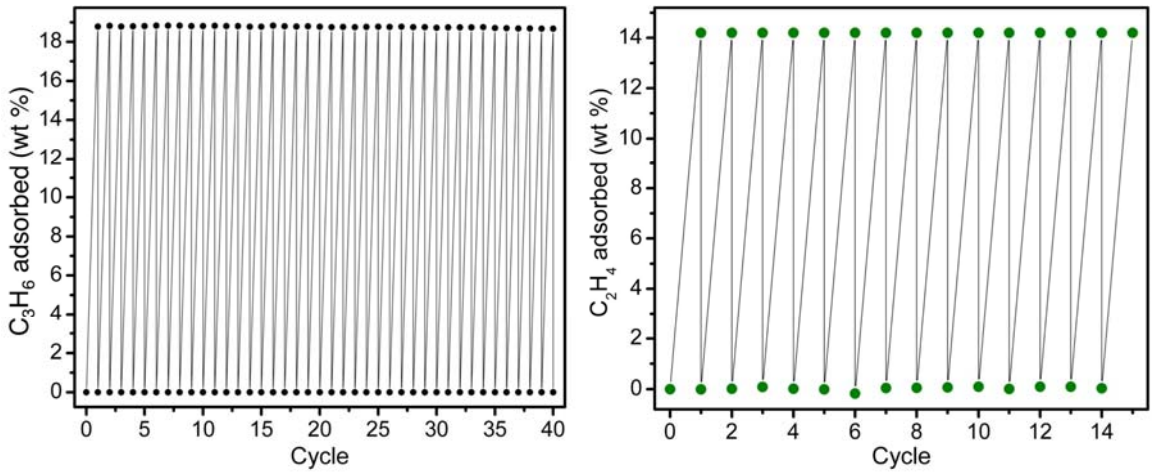

Fig. S2

Extended cycling of propylene adsorption in Fe_2(dobdc) via thermogravimetric analysis (left). Adsorption: pure propylene at 318 K, Desorption: nitrogen purge at 373 K. Cycling of ethylene in Fe_2(dobdc) via equilibrium adsorption measurements at 318 K. Desorption was achieved by placing the sample under dynamic vacuum at 373 K for 1 hour.

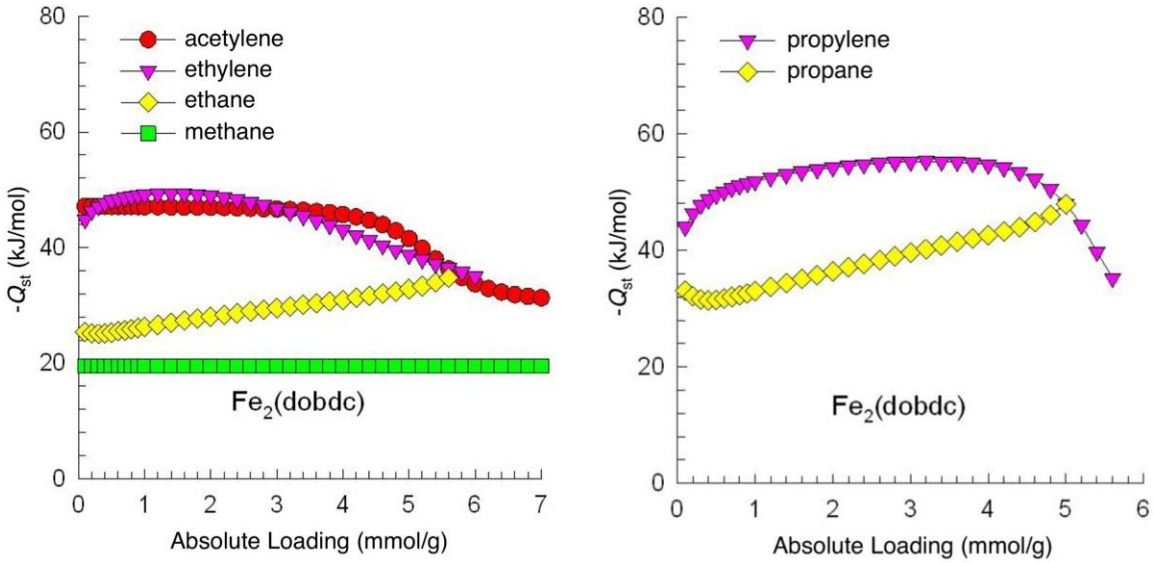

Fig. S3

Isosteric heats of hydrocarbon adsorption for methane, ethane, ethylene, and acetylene in Fe_2(dobdc) at 318 K, left. Isosteric heats of adsorption for propane ad propylene in Fe_2(dobdc) at 318 K, right.

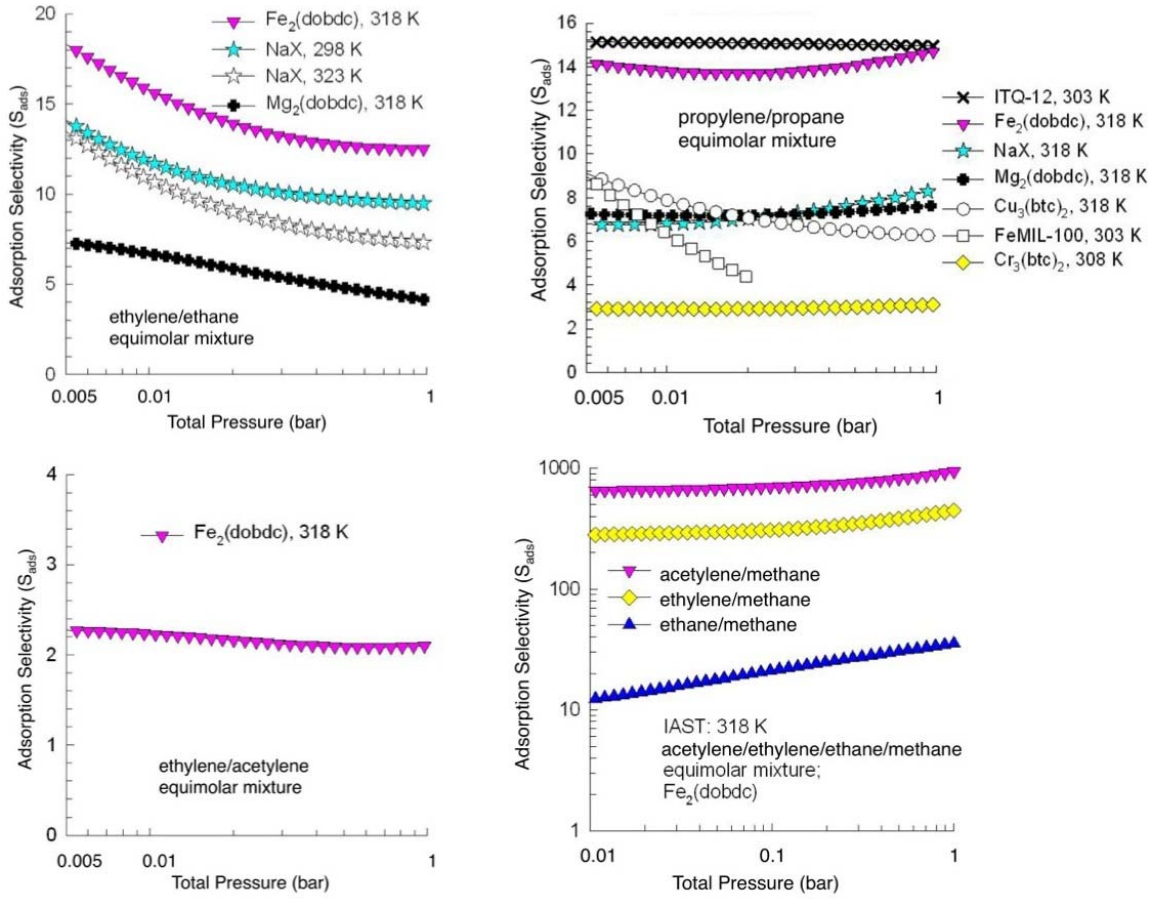

Fig. S4

Calculations of the adsorption selectivity, S_{ads}, using Ideal Adsorbed Solution Theory for ethane/ethylene (upper left), propane/propylene (upper right), acetylene/ethylene (lower left) and acetylene/methane, ethylene/methane, ethane/methane (lower right) in Fe_2(dobdc) at 318 K.

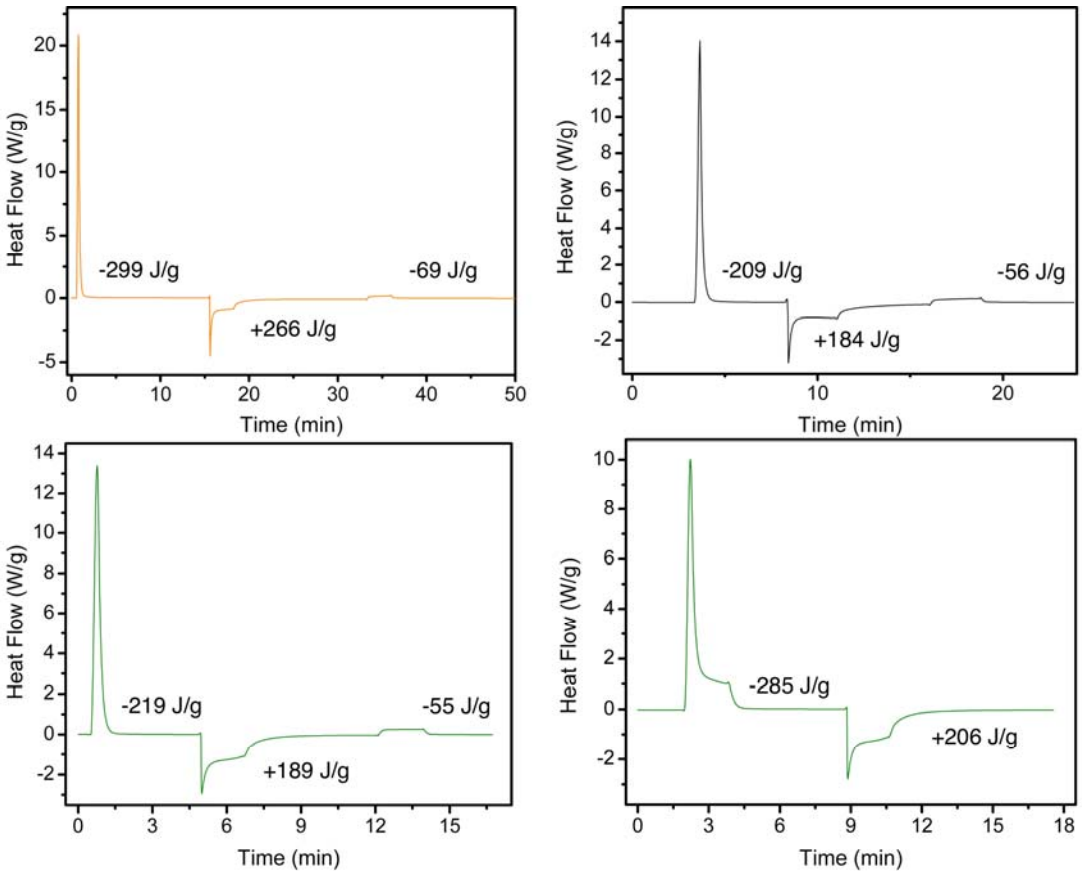

Fig. S5

Differential scanning calorimetry of hydrocarbon adsorption and desorption in Fe_2(dobdc) for acetylene (top left), propylene (top right), and ethylene (bottom left). The cycle consisted of adsorption of the hydrocarbon at 318 K, followed by heating under helium while ramping to 373 K, then cooling under helium to 318 K. The plot in the bottom right is adsorption of ethylene in Fe_2(dobdc) from 373 to 318 K, followed by purgin with helium while ramping to 373 K.

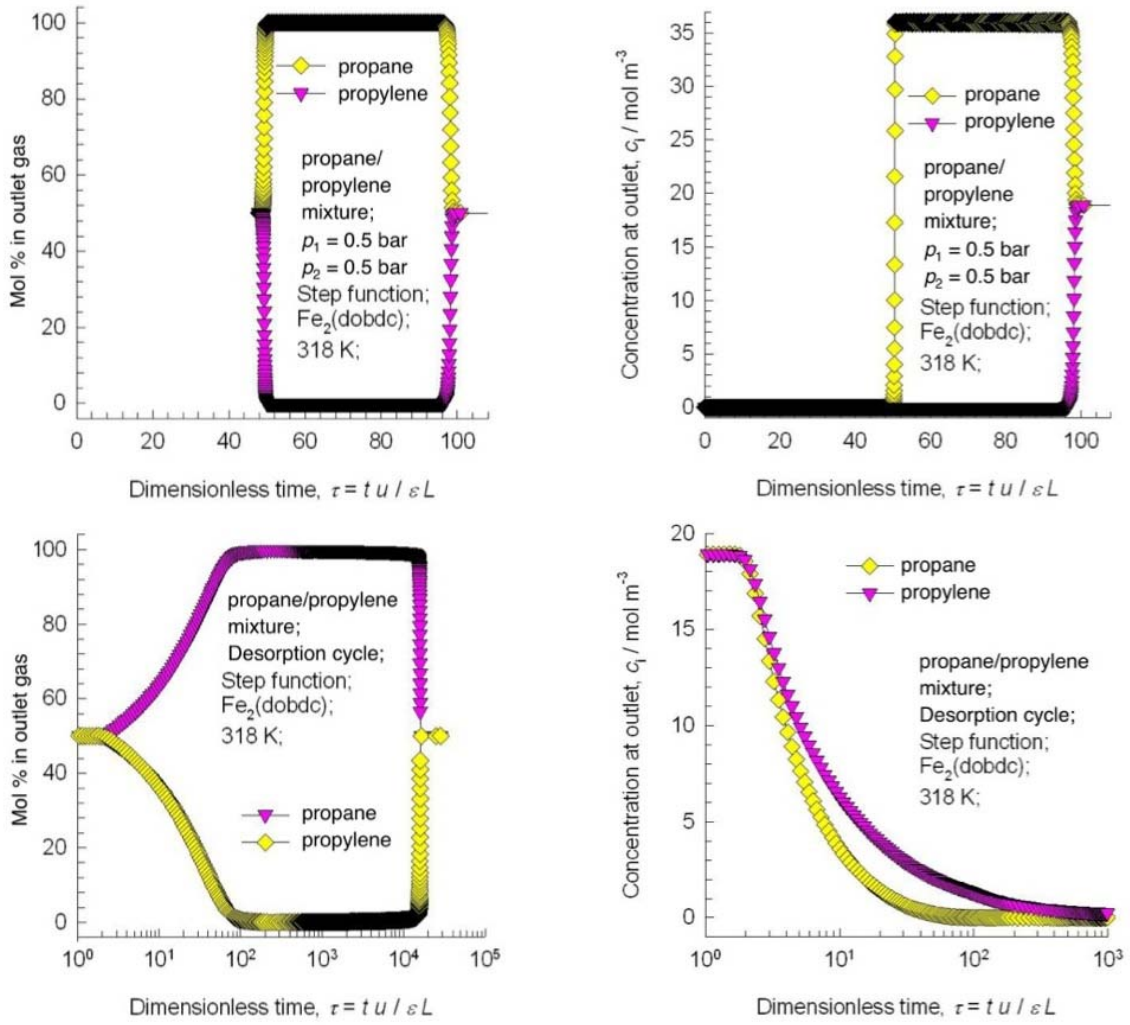

Fig. S6

Curves showing mol % (left) and concentration (right) of propane and propylene during adsorption (upper) and desorption (lower) of a simulated breakthrough experiment.

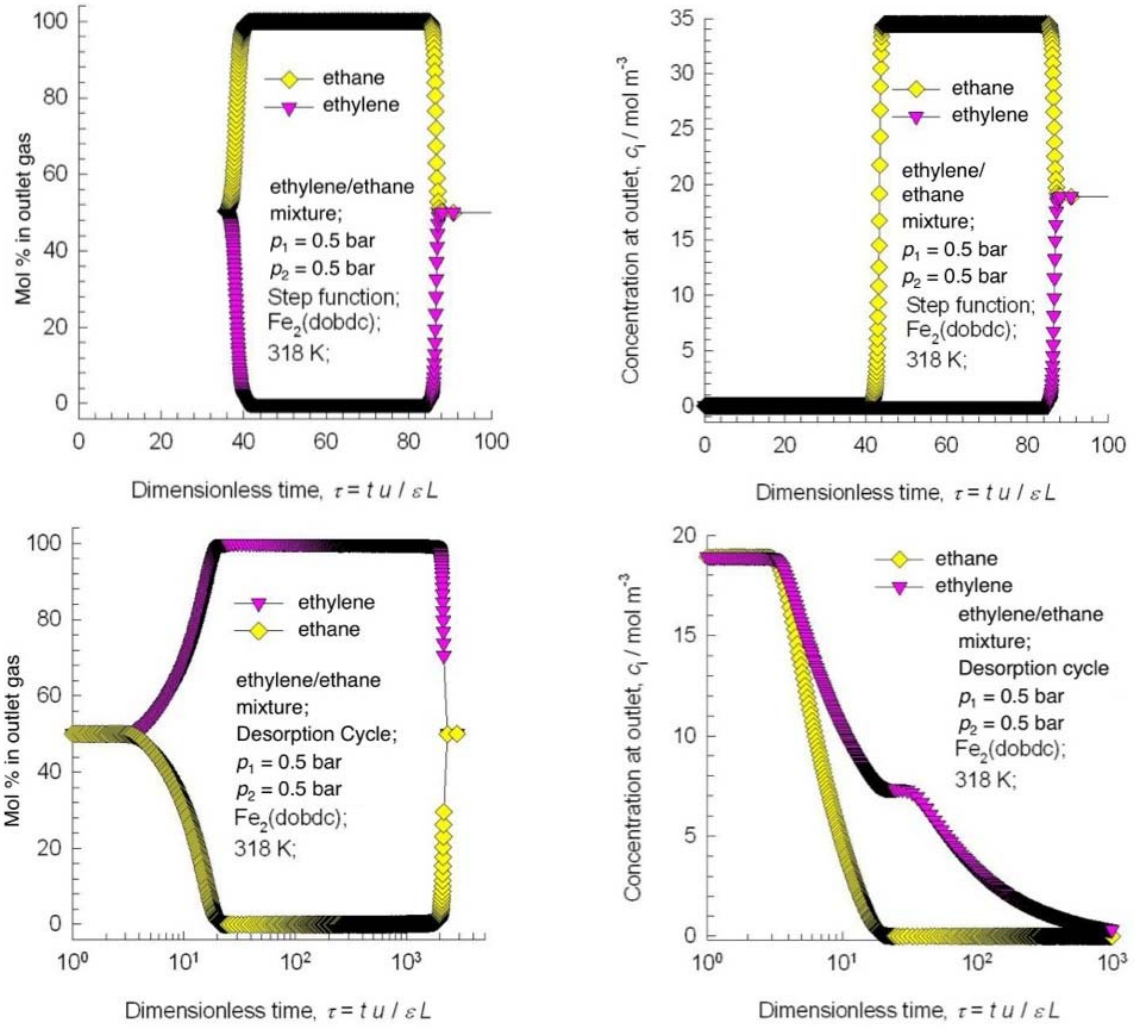

Fig. S7

Curves showing mol % (left) and concentration (right) of ethane and ethylene during adsorption (upper) and desorption (lower) of a simulated breakthrough experiment.

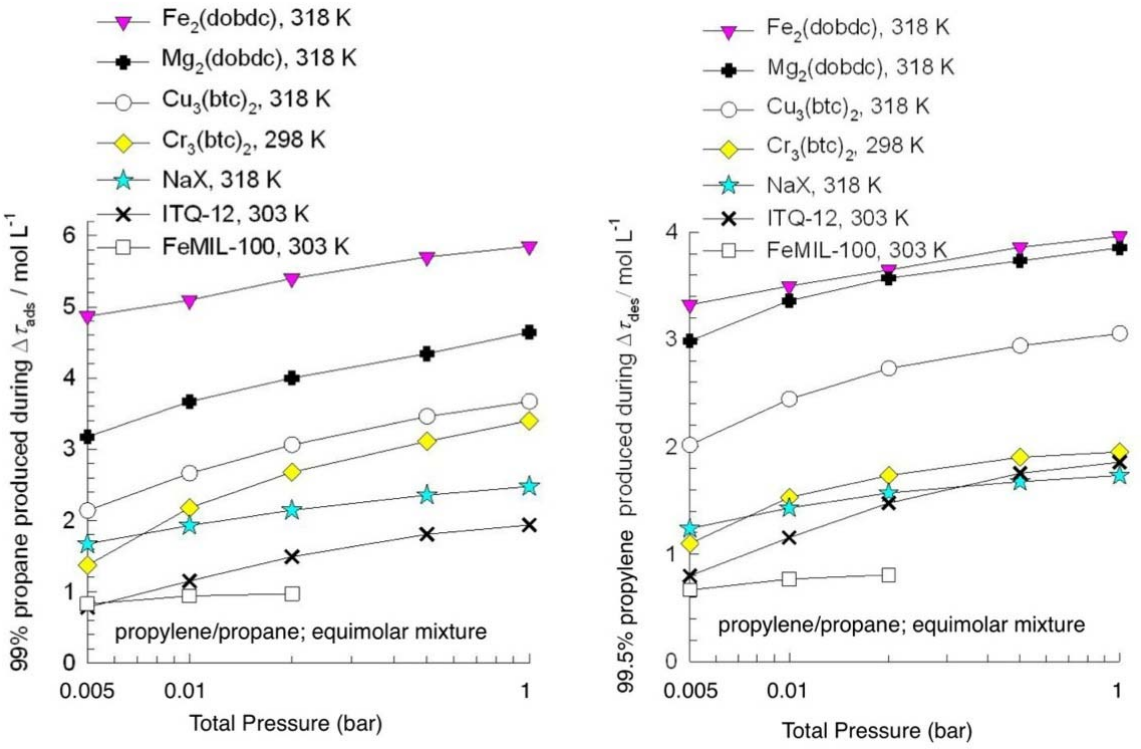

Fig. S8

Left - Production capacity of 99% pure propane, expressed as mol propane produced per L adsorbent material, as a function of the total pressure at the inlet to the adsorber. The separation characteristics of Fe_2(dobdc) at 318 K are compared to that of Mg_2(dobdc) (318 K), NaX zeolite (318 K), $Cu_3(btc)_2$ (318 K), $Cr_3(btc)_2$ (308 K), ITQ-12 (303 K), and FeMIL-100 (303 K). Right - Production capacity of 99% pure propane, expressed as mol propane produced per L adsorbent material, as a function of the total pressure at the inlet to the adsorber.

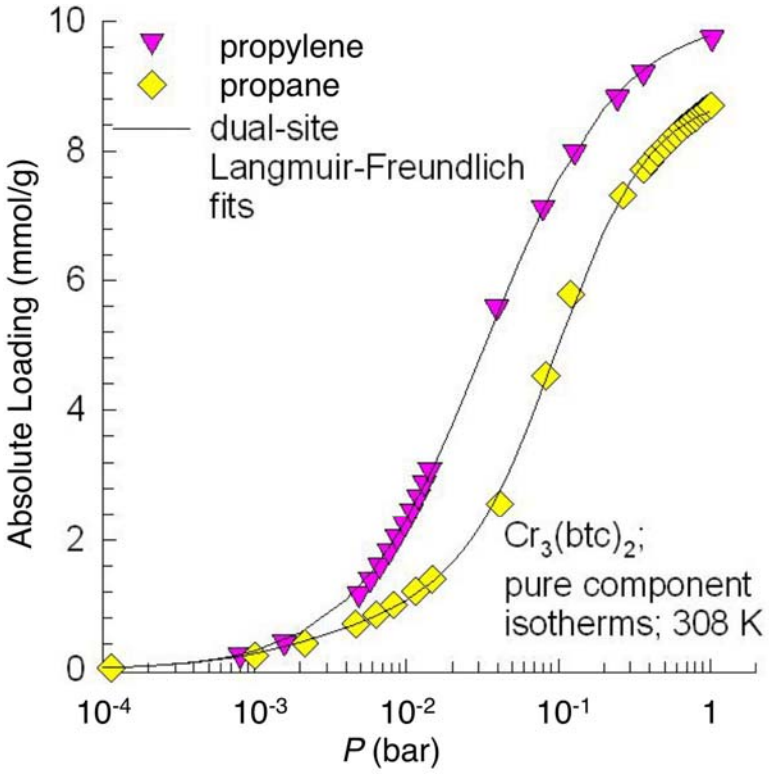

Fig. S9

The pure component isotherm data for propylene and propane in $Cr_3(btc)_2$ at 308 K. The continuous solid lines are the dual-Langmuir-Freundlich fits using the parameters specified in Table S13.

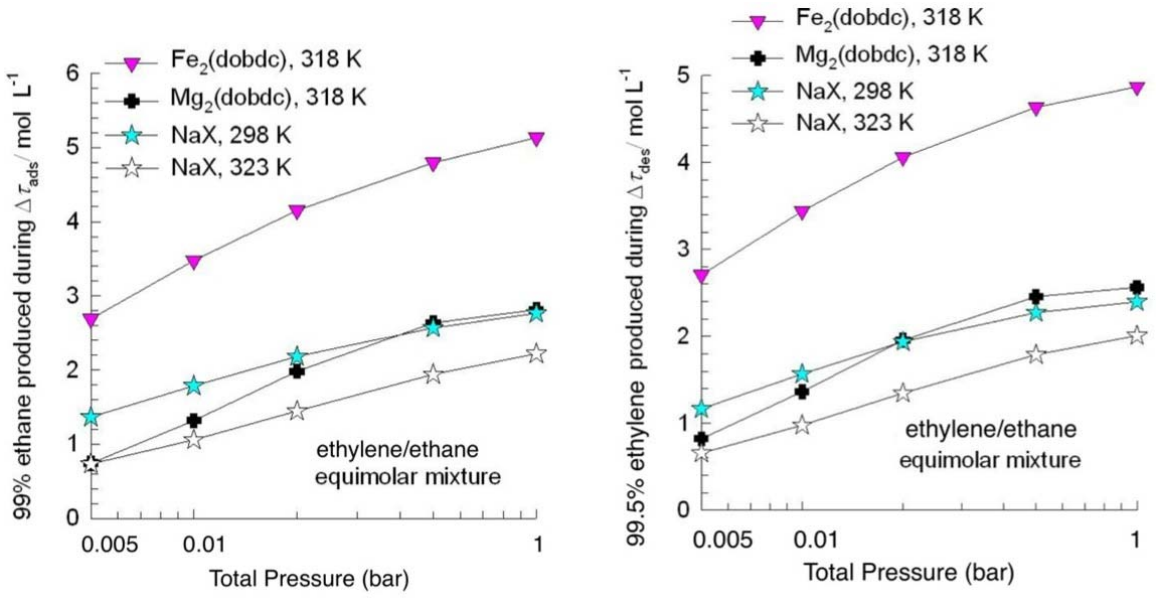

Fig. S10
Production capacities of 99% pure ethane (left), and 99.5% pure ethylene (right), expressed as mol produced per L adsorbent material, as a function of the total pressure at the inlet to the adsorber, as a function of the total pressure at the inlet to the adsorber. The separation characteristics of Fe_2(dobdc) at 318 K are compared to that of Mg_2(dobdc) (at 318 K), and NaX zeolite at temperatures of 298 K, and 323 K.

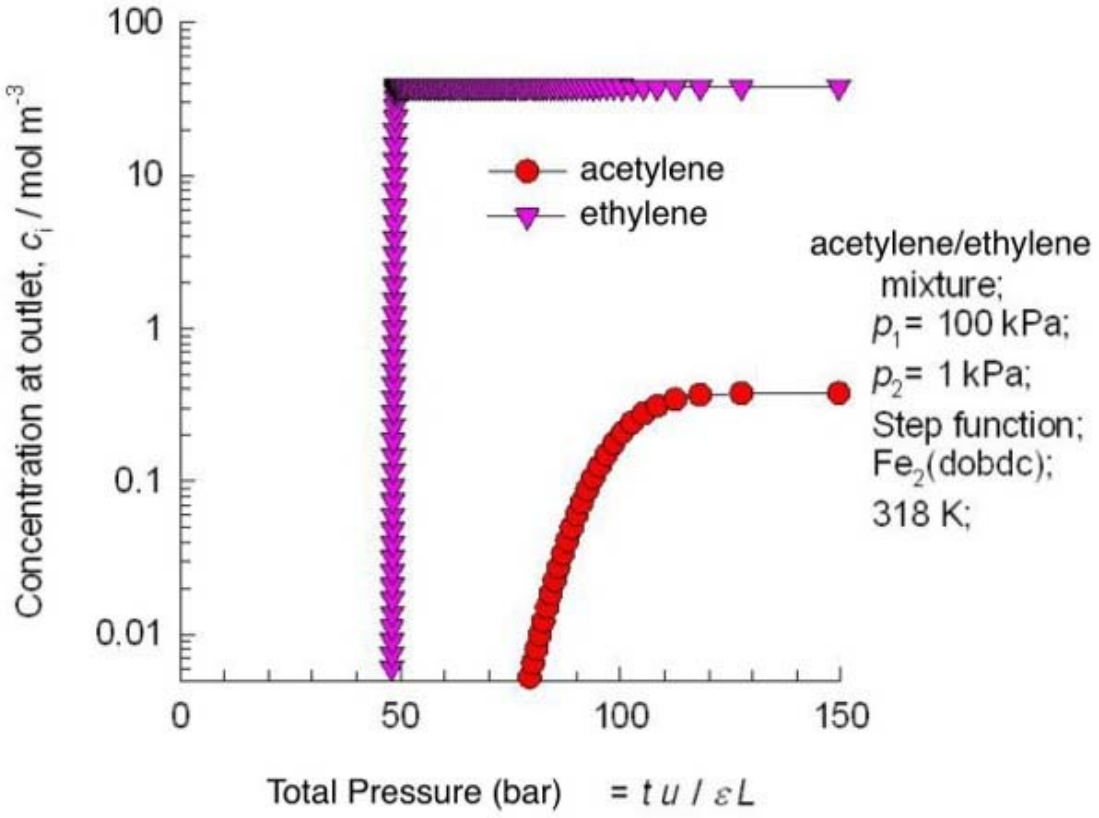

Fig. S11

Transient breakthrough of acetylene/ethylene mixture in an adsorber bed packed with Fe_2(dobdc).The inlet gas is maintained at partial pressures p_1 = 100 kPa, p_2 = 1 kPa, at a temperature of 318 K.

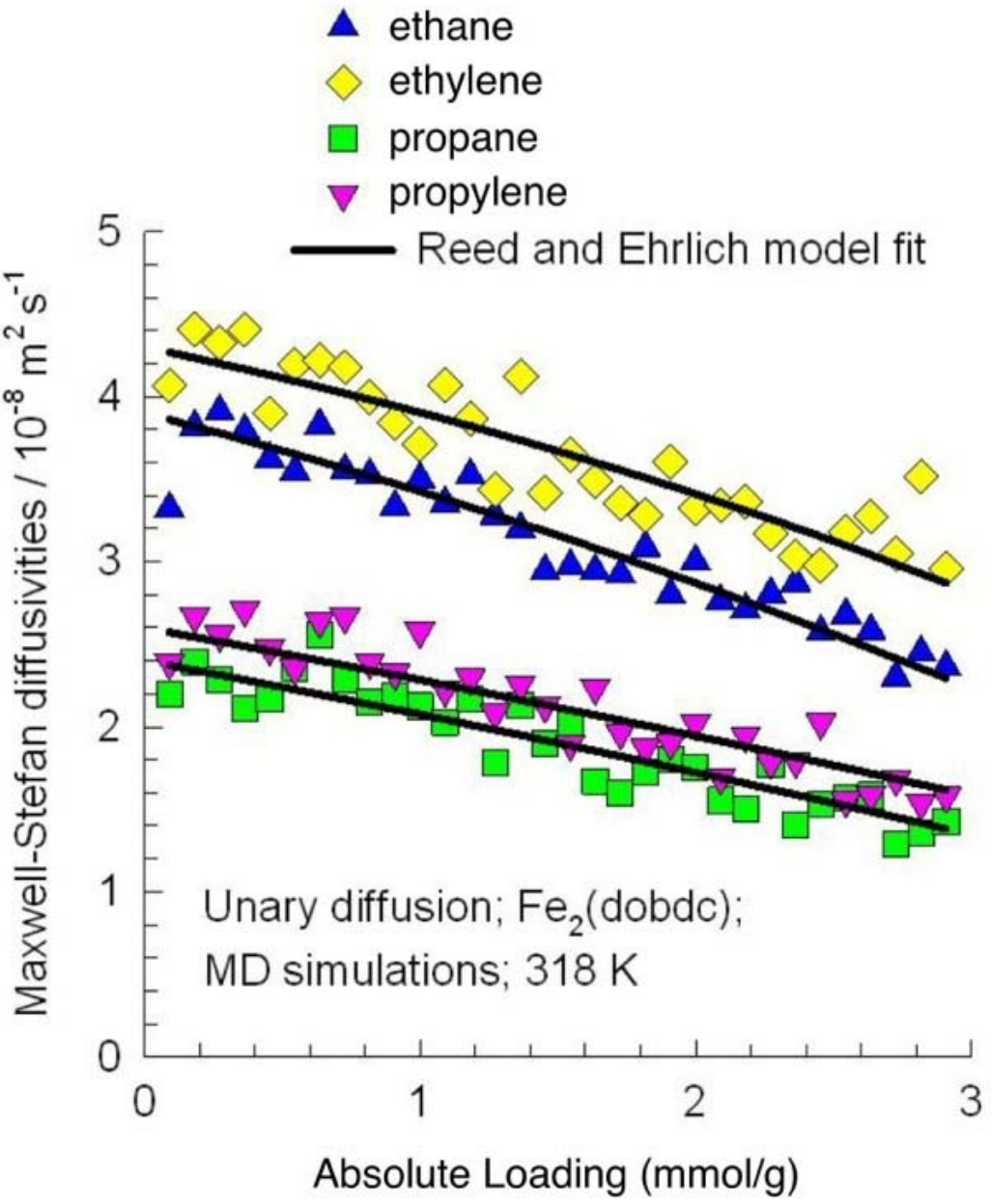

Fig. S12

MD simulations of the Maxwell-Stefan diffusivities for unary diffusion of ethylene, ethane, propylene, and propane in Fe_2(dobdc) at 318 K. The diffusivities are plotted as a function of the molar loadings. The continuous solid lines are the fits of the diffusivity data using the Reed and Ehrlich model [16,24,25]. The parameter values used are presented in Table S15.

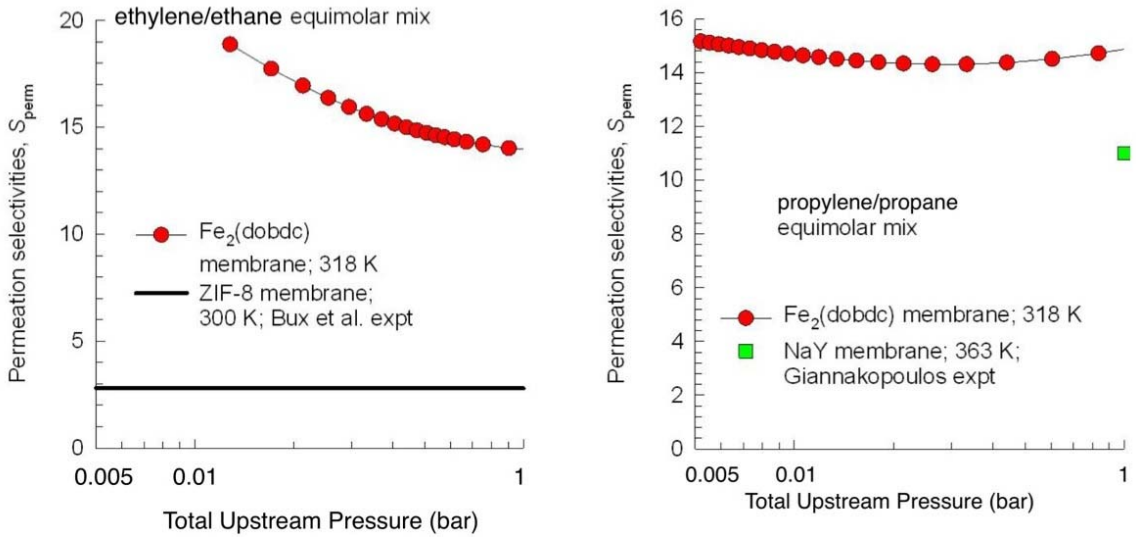

Fig. S13

(Left) The permeation selectivity, S_{perm}, for ethylene/ethane binary mixtures across Fe_2(dobdc) membrane at 318 K, plotted as a function of the total upstream pressure, $p_{t0} = p_{10} + p_{20}$. The partial pressures in the gas phase in the upstream compartment satisfy $p_{10}=p_{20}$. The downstream partial pressures were maintained at 10 Pa. The thickness of crystalline layer = 50 μm. Also plotted in this Figure are the selectivity values for ZIF-8, reported in the experimental work of Bux et al.(*31*)

(Right) The permeation selectivity, S_{perm}, for propylene/propane binary mixtures across Fe_2(dobdc) membrane at 318 K, plotted as a function of the total upstream pressure, $p_{t0} = p_{10} + p_{20}$. The partial pressures in the gas phase in the upstream compartment satisfy $p_{10}=p_{20}$. The downstream partial pressures were maintained at 10 Pa for each species. The thickness of crystalline layer = 50 μm. Also plotted in this Figure is the selectivity value for NaY membrane, reported in the experimental work of Giannakopoulos et al.(*41*)

Table S1.

Dual-site Langmuir-Freundlich parameters for pure acetylene isotherms in Fe_2(dobdc) at 318 K, 333 K, and 353 K.

	Site A			Site B		
	$q_{i,A,sat}$ mol/kg	$b_{i,A}$ $Pa^{-\nu_i}$	$\nu_{i,A}$ dimensionless	$q_{i,B,sat}$ mol/kg	$b_{i,B}$ $Pa^{-\nu_i}$	$\nu_{i,B}$ dimensionless
318 K	5.3	1.086×10^{-3}	1	3.6	8.69×10^{-6}	1
333 K	5.3	4.772×10^{-4}	1	3.6	4.776×10^{-6}	1
333 K	5.3	1.844×10^{-4}	1	3.6	2.782×10^{-6}	1

Table S2.

Dual-site Langmuir-Freundlich parameters for pure ethylene isotherms in Fe_2(dobdc) at 318 K, 333 K, and 353 K.

	Site A			Site B		
	$q_{i,A,sat}$ mol/kg	$b_{i,A}$ $Pa^{-\nu_i}$	$\nu_{i,A}$ dimensionless	$q_{i,B,sat}$ mol/kg	$b_{i,B}$ $Pa^{-\nu_i}$	$\nu_{i,B}$ dimensionless
318 K	3.6	3.71×10^{-4}	1.1	3.3	8.29×10^{-5}	1
333 K	3.6	1.28×10^{-4}	1.1	3.3	4.89×10^{-5}	1
333 K	3.6	2.98×10^{-5}	1.01	3.3	9.75×10^{-5}	1

Table S3.

Dual-site Langmuir-Freundlich parameters for pure ethane isotherms in Fe_2(dobdc) at 318 K, 333 K, and 353 K.

	Site A			Site B		
	$q_{i,A,sat}$ mol/kg	$b_{i,A}$ $Pa^{-\nu_i}$	$\nu_{i,A}$ dimensionless	$q_{i,B,sat}$ mol/kg	$b_{i,B}$ $Pa^{-\nu_i}$	$\nu_{i,B}$ dimensionless
318 K	5	1.71×10^{-8}	1.7	1	7.89×10^{-5}	1
333 K	5	2.19×10^{-8}	1.6	1	4.45×10^{-5}	1
333 K	5	2.59×10^{-8}	1.5	1	2.74×10^{-5}	1

Table S4.

Dual-site Langmuir-Freundlich parameters for pure propylene isotherms in Fe_2(dobdc) at 318 K, 333 K, and 353 K.

	Site A			Site B		
	$q_{i,A,sat}$ mol/kg	$b_{i,A}$ $Pa^{-\nu_i}$	$\nu_{i,A}$ dimensionless	$q_{i,B,sat}$ mol/kg	$b_{i,B}$ $Pa^{-\nu_i}$	$\nu_{i,B}$ dimensionless
318 K	5.2	7.7×10^{-4}	1.42	1.8	1.21×10^{-4}	1
333 K	6	4.12×10^{-4}	1.26	1.4	2.06×10^{-5}	1
333 K	5.9	1.56×10^{-4}	1.2	1.1	2.01×10^{-5}	1

Table S5.

Dual-site Langmuir-Freundlich parameters for pure propane isotherms in Fe_2(dobdc) at 318 K, 333 K, and 353 K.

	Site A			Site B		
	$q_{i,A,sat}$ mol/kg	$b_{i,A}$ $Pa^{-\nu_i}$	$\nu_{i,A}$ dimensionless	$q_{i,B,sat}$ mol/kg	$b_{i,B}$ $Pa^{-\nu_i}$	$\nu_{i,B}$ dimensionless
318 K	2.4	4.04×10^{-10}	2.85	3.9	1.93×10^{-4}	1
333 K	2.2	1.1×10^{-9}	2.53	3.9	1.13×10^{-4}	1
333 K	2.2	8.28×10^{-9}	2.08	3.6	5.74×10^{-5}	1

Table S6.

Parameters for single-site Langmuir model $q = \frac{q_{sat} bp}{1 + bp}$ adsorption of CH_4 in Fe_2(dobdc) at 318 K, 333 K, and 353 K.

	q_{sat} mol/kg	b Pa^{-1}	b_0 Pa^{-1}	E kJ/mol
CH_4	5	$b = b_0 \exp\left(\frac{E}{RT}\right)$	1.13×10^{-9}	19.5

Table S7.

Dual-site Langmuir-Freundlich parameters for pure ethylene isotherms in NaX zeolite at 298 K, and 323 K. The experimental data are from Hyun and Danner.

	Site A			Site B		
	$q_{i,A,sat}$ mol/kg	$b_{i,A}$ $Pa^{-\nu_i}$	$\nu_{i,A}$ dimensionless	$q_{i,B,sat}$ mol/kg	$b_{i,B}$ $Pa^{-\nu_i}$	$\nu_{i,B}$ dimensionless
298 K	1.5	1.23×10^{-2}	0.55	1.5	1.02×10^{-4}	1.06
323 K	1.5	4.86×10^{-3}	0.55	1.5	4.24×10^{-5}	1.06

Table S8.

Dual-site Langmuir-Freundlich parameters for pure ethane isotherms in NaX zeolite at 298 K, and 323 K. The experimental data are from Hyun and Danner.

	Site A			Site B		
	$q_{i,A,sat}$ mol/kg	$b_{i,A}$ $Pa^{-\nu_i}$	$\nu_{i,A}$ dimensionless	$q_{i,B,sat}$ mol/kg	$b_{i,B}$ $Pa^{-\nu_i}$	$\nu_{i,B}$ dimensionless
298 K	1.5	2.75×10^{-4}	0.73	1.5	2.7×10^{-7}	1.54
323 K	1.5	1.71×10^{-4}	0.73	1.4	6.38×10^{-8}	1.54

Table S9.

Dual-site Langmuir-Freundlich parameters for propylene and propane isotherms in NaX zeolite at 318 K. The parameter fits are based on re-fitting the data provided in Table 4 of the paper by Lamia et al.

	Site A			Site B		
	$q_{i,A,sat}$ mol/kg	$b_{i,A}$ $Pa^{-\nu_i}$	$\nu_{i,A}$ dimensionless	$q_{i,B,sat}$ mol/kg	$b_{i,B}$ $Pa^{-\nu_i}$	$\nu_{i,B}$ dimensionless
propylene	1.1	4.47×10^{-3}	1	1.44	3.4×10^{-4}	1
propane	1.1	1.28×10^{-4}	1	1.1	4.44×10^{-4}	1

Table S10.

Single-site Langmuir-Freundlich parameters for propylene and propane isotherms in FeMIL-100 at 303 K. The parameter fits are based on fitting the data provided in Figure 2 of the paper by Yoon et al.

	$q_{i,A,sat}$ mol/kg	$b_{i,A}$ $Pa^{-\nu_i}$	$\nu_{i,A}$ dimensionless
propylene	2.1	6.21×10^{-3}	0.64
propane	7	1.53×10^{-5}	1

Table S11.

Single-site Langmuir-Freundlich parameters for propylene and propane isotherms in ITQ-12 at 303 K. The parameter fits are based on fitting the data provided in the paper by Gutiérrez-Sevillano et al.

	$q_{i,A,sat}$ mol/kg	$b_{i,A}$ $Pa^{-\nu_i}$	$\nu_{i,A}$ dimensionless
propylene	1.4	2.38×10^{-4}	1
propane	1.41	1.56×10^{-5}	1

Table S12.

Dual-site Langmuir-Freundlich parameters for propylene and propane isotherms in $Cu_3(btc)_2$ at 318 K. The parameter fits are based on Table 3 of the paper by Plaza et al.

	Site A			Site B		
	$q_{i,A,sat}$ mol/kg	$b_{i,A}$ $Pa^{-\nu_i}$	$\nu_{i,A}$ dimensionless	$q_{i,B,sat}$ mol/kg	$b_{i,B}$ $Pa^{-\nu_i}$	$\nu_{i,B}$ dimensionless
propylene	5.6	5.37×10^{-4}	1	0.96	7.45×10^{-6}	1.25
propane	4.9	1.05×10^{-5}	1.2195	0.9	2.56×10^{-12}	3.125

Table S13.

Dual-site Langmuir-Freundlich parameters for propylene and propane isotherms in $Cr_3(btc)_2$ at 308 K.

	Site A			Site B		
	$q_{i,A,sat}$ mol/kg	$b_{i,A}$ $Pa^{-\nu_i}$	$\nu_{i,A}$ dimensionless	$q_{i,B,sat}$ mol/kg	$b_{i,B}$ $Pa^{-\nu_i}$	$\nu_{i,B}$ dimensionless
propylene	8.2	2.98×10^{-4}	1	1.9	2.98×10^{-4}	1
propane	7.9	2.62×10^{-6}	1.4	1	3.14×10^{-3}	1

Table S14.

The alkane-alkane interactions were determined using the force field of Dubbeldam et al.(*42*) The alkene-alkene interactions were determined using the force field of Ban et al.(*43*) The metal-organic framework structure was considered to be rigid in the simulations. For the atoms in the Fe_2(dobdc), the generic UFF(*44*) and DREIDING(45) force fields were used to determine the Lennard-Jones parameters given below. The framework charges were estimated using the quantum chemical calculations with the software provided in *Materials Studio*, Accelrys, San Diego. The Lorentz-Berthelot mixing rules were applied for calculating for guest-host interactions.

(pseudo-) atom	σ / Å	ε/k_B / K	charge
Fe	27.68	4.04	0.2846
O_A	48.16	3.03	-0.1215
O_B	48.16	3.03	-0.1778
O_C	48.16	3.03	-0.176
C_A	47.86	3.47	0.1917
C_B	47.86	3.47	-0.0374
C_C	47.86	3.47	0.0723
C_D	47.86	3.47	-0.0661
H	7.65	2.85	0.0301

Table S15.

Reed-Ehrlich parameters for a variety of species in Fe_2(dobdc) at 318 K.

Molecule	$Đ_i(0)$ / 10^{-8} m^2 s^{-1}	Coordination number	ϕ_i
ethane	3.9	2	1.2
ethylene	4.3	2	1.3
propane	2.4	2	1.1
propylene	2.6	2	1.1

Table S16.

The degree of correlations, $Đ_i/Đ_{ii,}$ in Fe_2(dobdc) at 318 K were fitted using the constants specified below.

Molecule	$Đ_i/Đ_{ii}$
ethane	1.2
ethylene	1.2
propane	1.2
propylene	1.2

Table S17.

Parameters used to fit susceptibility curves for hydrocarbons adsorbed in Fe_2(dobdc)

	g_{iso}	J (cm^{-1})	J' (cm^{-1})
Activated	2.083(3)	4.12(6)	–1.12(1)
CH_4	2.015(4)	3.3(1)	–0.95(1)
C_2H_6	2.043(4)	3.19(8)	–0.97(1)
C_3H_8	1.99(2)	3.0(3)	–1.00(5)
C_2H_2	2.14(1)	–3.1(3)	-1.1(3)
C_2H_4	2.17(1)	–3.9(2)	-1.1(3)
C_3H_6	2.146(1)	–1.11(7)	-1.18(7)

Table S18.

Rietveld refinement results (9 K data) of bare Fe_2(dobdc). Values in parenthesis indicate one standard deviation of the parameter value.

Space group R-3, *a* = 26.0983(5) Å, *c* = 6.8512(2) Å, cell volume = 4041.3(1) Å.

Goodness-of-fit parameters: wRp = 3.59 %, Rp = 2.82 %, reduced χ^2 = 2.84.

Atom	x	y	Z	Multiplicity	Occupancy	Uiso (Å^2)
Fe	0.3824(2)	0.3521(2)	0.1430(6)	18	1.0	0.012(2)
O1	0.3272(3)	0.2938(4)	0.363(1)	18	1.0	0.003(3)
O2	0.3010(4)	0.2272(4)	0.599(2)	18	1.0	0.023(3)
O3	0.3551(4)	0.2732(4)	0.007(1)	18	1.0	0.009(2)
C1	0.3161(4)	0.2440(4)	0.421(1)	18	1.0	0.022(2)
C2	0.3259(4)	0.2038(3)	0.286(1)	18	1.0	0.002(2)
C3	0.3430(3)	0.2226(4)	0.095(1)	18	1.0	0.012(2)
C4	0.3487(3)	0.1819(4)	-0.034(1)	18	1.0	0.003(2)
H	0.3613(6)	0.1919(6)	-0.168(2)	18	1.0	0.01(1)

Table S19.

Rietveld Refinement (9 K data) of Fe_2(dobdc)-0.5(ethane).
Space group R-3, *a* = 26.0836(5) Å, *c* = 6.8551(2) Å, cell volume = 4039.1(2) Å.
Goodness-of-fit parameters: wRp = 4.35 %, Rp = 3.44 %, reduced χ^2 = 2.215.

Atom	X	Y	Z	Occupancy	Uiso(Å)^2	Multiplicity
Fe	0.3810(2)	0.3508(2)	0.1434(6)	1	0.0118(9)	18
O1	0.3263(4)	0.2949(4)	0.354(1)	1	0.021(3)	18
O2	0.3022(4)	0.2293(4)	0.591(1)	1	0.033(3)	18
O3	0.3491(4)	0.2747(3)	0.009(1)	1	0.004(2)	18
C1	0.3164(3)	0.2452(3)	0.420(1)	1	0.006(2)	18
C2	0.3251(3)	0.2042(3)	0.287(1)	1	0.007(2)	18
C3	0.3414(3)	0.2229(3)	0.086(1)	1	0.006(2)	18
C4	0.3487(3)	0.1794(4)	-0.030(1)	1	0.011(2)	18
H	0.3649(5)	0.1922(6)	-0.171(2)	1	0.008(3)	18
C1a	0.5244(8)	0.8465(8)	0.651(3)	0.466(3)	0.048(5)	18
C2a	0.5110(8)	0.8571(8)	0.850(3)	0.466(3)	0.048(5)	18
D3	0.491(1)	0.803(1)	0.604(3)	0.466(3)	0.077(3)	18
D4	0.526(1)	0.8793(9)	0.555(3)	0.466(3)	0.077(3)	18
D5	0.5681(8)	0.8522(9)	0.646(4)	0.466(3)	0.077(3)	18
D6	0.5452(9)	0.899(1)	0.902(3)	0.466(3)	0.077(3)	18
D7	0.469(1)	0.8554(8)	0.853(4)	0.466(3)	0.077(3)	18
D8	0.5101(9)	0.8242(9)	0.948(3)	0.466(3)	0.077(3)	18

Table S20.

Rietveld refinement results (9 K data) of Fe_2(dobdc)-0.75(ethylene).
Space group R-3, *a* = 25.8784(9) Å, *c* = 6.9669(4) Å, cell volume = 4040.6(3) Å.
Goodness-of-fit parameters: wRp = 3.92 %, Rp = 3.10 %, reduced χ^2 = 1.855.

Atom	X	Y	Z	Occupancy	Uiso(Å)^2	Multiplicity
Fe	0.3877(4)	0.3523(4)	0.145(1)	1	0.008(3)	18
O1	0.3183(5)	0.2939(5)	0.349(2)	1	0.003(4)	18
O2	0.3044(5)	0.2275(6)	0.595(2)	1	0.006(4)	18
O3	0.3558(6)	0.2748(6)	0.006(2)	1	0.004(5)	18
C1	0.3167(6)	0.2471(6)	0.419(2)	1	0.003(3)	18
C2	0.3254(6)	0.2055(6)	0.284(2)	1	0.001(3)	18
C3	0.3431(7)	0.2248(7)	0.095(2)	1	0.040(5)	18
C4	0.3496(5)	0.1813(6)	-0.016(2)	1	0.002(4)	18
H	0.365(1)	0.195(1)	-0.169(3)	1	0.016(7)	18
C11	0.9712(9)	0.7895(8)	0.853(3)	0.735(7)	0.023(7)	18
C12	1.000(1)	0.789(1)	1.001(3)	0.735(7)	0.024(8)	18
D1a	0.922(1)	0.7684(9)	0.867(3)	0.735(7)	0.062(9)	18
D2b	1.048(1)	0.818(1)	1.001(3)	0.735(7)	0.05(1)	18
D2a	0.9787(8)	0.775(1)	1.140(3)	0.735(7)	0.06(1)	18
D1b	0.9898(9)	0.8142(8)	0.7293(25)	0.735(7)	0.029(7)	18

Table S21.

Rietveld refinement results (9 K data) of Fe_2(dobdc)-acetylene.
Space group R-3, *a* = 25.9202(5) Å, *c* = 6.9505(2) Å, cell volume = 4044.1(2) Å.
Goodness-of-fit parameters: wRp = 3.46 %, Rp = 2.77 %, reduced χ^2 = 1.964

Atom	X	Y	Z	Occupancy	Uiso(Å)^2	Multiplicity
Fe	0.3862(2)	0.3515(2)	0.1485(6)	1	0.0065(9)	18
O1	0.3184(3)	0.2922(3)	0.348(1)	1	0.0034(9)	18
O2	0.3026(3)	0.2265(3)	0.592(1)	1	0.0034(9)	18
O3	0.3529(3)	0.2711(3)	0.009(1)	1	0.0034(9)	18
C1	0.3141(3)	0.2458(2)	0.423(1)	1	0.0064(6)	18
C2	0.3276(3)	0.2059(3)	0.282(1)	1	0.0085(6)	18
C3	0.3435(3)	0.2214(3)	0.0912(9)	1	0.0080(6)	18
C4	0.3510(3)	0.1810(3)	-0.0272(9)	1	0.0108(6)	18
H	0.3604(5)	0.1913(5)	-0.175(2)	1	0.007(3)	18
C5	0.1466(2)	0.6872(3)	0.530(1)	0.856(4)	0.028(2)	18
C6	0.1225(2)	0.6706(3)	0.678(1)	0.856(4)	0.028(2)	18
D1	0.1697(3)	0.6992(5)	0.399(1)	0.856(4)	0.120(6)	18
D2	0.1049(3)	0.6540(4)	0.816(1)	0.856(4)	0.053(4)	18

Table S22.

Rietveld refinement results (9 K data) of Fe_2(dobdc)-0.75(propane).
Space group R-3, *a* = 26.0468(6) Å, *c* = 6.8282(2) Å, cell volume = 4011.8(2) Å.
Goodness-of-fit parameters: wRp = 4.43%, Rp = 3.60 %, reduced χ^2 = 1.819

Atom	X	Y	Z	Occupancy			Multiplicity
Fe	0.3799(3)	0.3482(3)	0.1455(9)	1	Uiso	0.012(1)	18
O1	0.3278(5)	0.2944(4)	0.350(2)	1	Uiso	0.022(4)	18
O2	0.3025(5)	0.2197(5)	0.567(2)	1	Uiso	0.022(3)	18
O3	0.3453(5)	0.2675(4)	0.007(2)	1	Uiso	0.022(3)	18
C1	0.3174(4)	0.2452(4)	0.416(1)	1	Uiso	0.002(2)	18
C2	0.3289(4)	0.2059(3)	0.300(1)	1	Uiso	0.002(2)	18
C3	0.3431(4)	0.2241(4)	0.091(1)	1	Uiso	0.002(2)	18
C4	0.3494(4)	0.1811(4)	-0.025(1)	1	Uiso	0.002(2)	18
H	0.3657(6)	0.1988(6)	-0.1630(3)	1	Uiso	0.001(4)	18
C1a	0.5236(8)	0.8635(8)	0.646(2)	0.617(2)	Uani	0.040*	18
C2a	0.5027(8)	0.8566(8)	0.853(3)	0.617(2)	Uani	0.048*	18
D4	0.5103(8)	0.8872(7)	0.556(3)	0.617(2)	Uani	0.050*	18
D5	0.5690(6)	0.8772(7)	0.645(2)	0.617(2)	Uani	0.049*	18
D6	0.5335(9)	0.8923(8)	0.937(4)	0.617(2)	Uani	0.116*	18
D7	0.4655(8)	0.8618(6)	0.867(4)	0.617(2)	Uani	0.099*	18
D8	0.499(1)	0.8181(9)	0.924(3)	0.617(2)	Uani	0.185*	18
C3a	0.4909(9)	0.804(1)	0.570(6)	0.617(2)	Uani	0.292*	18
D9	0.458(2)	0.793(2)	0.458(6)	0.617(2)	Uani	0.582*	18
D10	0.4695(7)	0.7786(7)	0.708(6)	0.617(2)	Uani	0.328*	18
D11	0.519(1)	0.788(3)	0.502(7)	0.617(2)	Uani	0.700*	18

*****Uaniso C1a = [U_{11} U_{12} U_{13} U_{22} U_{23} U_{33}] = [0.04(1) 0.021(7) 0.00(1) 0.04(1) 0.00(1) 0.04(1)]
Uaniso C2a = [U_{11} U_{12} U_{13} U_{22} U_{23} U_{33}] = [0.05(1) 0.021(9) -0.00(1) 0.05(1) -0.00(1) 0.04(1)]
Uaniso D4 = [U_{11} U_{12} U_{13} U_{22} U_{23} U_{33}] = [0.06(1) 0.026(9) -0.02(1) 0.05(1) -0.04(1) 0.04(1)]
Uaniso D5 = [U_{11} U_{12} U_{13} U_{22} U_{23} U_{33}] = [0.027(9) 0.025(7) 0.047(7) 0.08(1) -0.051(8) 0.03(1)]
Uaniso D6 = [U_{11} U_{12} U_{13} U_{22} U_{23} U_{33}] = [0.14(2) 0.078(8) 0.04(2) 0.03(1) 0.05(2) 0.22(3)]
Uaniso D7 = [U_{11} U_{12} U_{13} U_{22} U_{23} U_{33}] = [0.12(1) 0.090(7) -0.06(2) 0.048(9) -0.09(1) 0.19(2)]
Uaniso D8 = [U_{11} U_{12} U_{13} U_{22} U_{23} U_{33}] = [0.20(2) 0.03(1) 0.04(2) 0.12(2) -0.16(1) 0.18(2)]
Uaniso C3a = [U_{11} U_{12} U_{13} U_{22} U_{23} U_{33}] = [0.02(1) 0.09(1) -0.01(2) 0.29(2) 0.21(3) 0.59(5)]
Uaniso D9 = [U_{11} U_{12} U_{13} U_{22} U_{23} U_{33}] = [0.52(5) 0.29(3) -0.08(5) 0.48(4) 0.40(4) 0.80(9)]
Uaniso D10 = [U_{11} U_{12} U_{13} U_{22} U_{23} U_{33}] = [0.129(9) 0.158(6) 0.12(2) 0.17(1) -0.13(2) 0.80(6)]
Uaniso D11 = [U_{11} U_{12} U_{13} U_{22} U_{23} U_{33}] = [0.18(5) 0.00(6) -0.15(5) 0.80(1) 0.35(1) 0.80(1)]

For propane in Fe_2(dobdc) the adsorbed hydrocarbon molecule has orientational disorder with respect to the open metal center. Of several refined models, the single-molecule with large displacement parameters is the most reasonab**le.**

Table S23.
Rietveld refinement results (9 K data) of Fe_2(dobdc)- 0.75(propylene).
Space group R-3, *a* = 25.8998(9) Å, *c* = 6.9448(3) Å, cell volume = 4033.8(3) Å.
Goodness-of-fit parameters: wRp = 3.81%, Rp = 3.14 %, reduced χ^2 = 2.821

Atom	X	Y	Z	Occupancy			Multiplicity
Fe	0.3865(4)	0.3531(4)	0.157(1)	1	Uiso	0.015(3)	18
O1	0.3174(5)	0.2935(6)	0.356(2)	1	Uiso	0.003(2)	18
O2	0.3046(6)	0.2337(6)	0.591(2)	1	Uiso	0.002(2)	18
O3	0.3561(6)	0.2773(6)	0.002(2)	1	Uiso	0.008(2)	18
C1	0.3218(6)	0.2466(6)	0.416(2)	1	Uiso	0.025(2)	18
C2	0.3257(6)	0.2042(5)	0.282(2)	1	Uiso	0.002(2)	18
C3	0.3388(6)	0.2229(5)	0.090(2)	1	Uiso	0.006(2)	18
C4	0.3502(5)	0.1812(6)	-0.016(2)	1	Uiso	0.003(2)	18
H	0.368(1)	0.188(1)	-0.177(4)	1	Uiso	0.036(9)	18
C11	0.9664(9)	0.7912(9)	0.841(3)	0.699(5)	Uiso	0.019(5)	18
C12	0.9983(9)	0.7964(8)	0.998(2)	0.699(5)	Uiso	0.009(5)	18
D1a	0.9204(8)	0.7694(8)	0.839(3)	0.699(5)	Uiso	0.002(4)	18
D2b	1.0446(7)	0.8186(7)	0.988(2)	0.699(5)	Uiso	0.005(4)	18
D2a	0.9787(8)	0.7691(8)	1.112(2)	0.699(5)	Uiso	0.003(4)	18
D3a	0.980(2)	0.869(1)	0.686(5)	0.699(5)	Uiso	0.096(4)	18
D3b	0.977(1)	0.814(1)	0.538(4)	0.699(5)	Uiso	0.061(4)	18
D3c	1.0373(8)	0.8559(9)	0.680(2)	0.699(5)	Uiso	0.004(4)	18
C13	0.993(2)	0.835(2)	0.679(7)	0.699(5)	Uani	0.34398*	18

Movie S1
MD simulation of ethane/ethylene in the channels of an Fe_2(dobdc) membrane at 318 K.

Movie S2
MD simulation of propane/propylene in the channels of an Fe_2(dobdc) membrane at 318 K.

Movie S3
Simulated breakthrough for the adsorption of ethane and ethylene in Fe_2(dobdc) at 318 K.

Movie S4
Simulated breakthrough for the desorption of ethane and ethylene in Fe_2(dobdc) at 318 K.

Movie S5
Simulated breakthrough for the adsorption of ethane and ethylene in zeolite NaX at 298 K.

Movie S6
Simulated breakthrough for the desorption of ethane and ethylene in zeolite NaX at 298 K.

Movie S7
Simulated breakthrough for the adsorption of an equimolar methane/ethane/ethylene/acetylene mixture in Fe_2(dobdc) at 318 K.

Movie S8
Simulated breakthrough for the adsorption of propane and propylene in Fe_2(dobdc) at 318 K.

Movie S9
Simulated breakthrough for the desorption of propane and propylene in Fe_2(dobdc) at 318 K.

Movie S10
Simulated breakthrough for the adsorption of propane and propylene in zeolite NaX at 318 K.

Movie S11
Simulated breakthrough for the desorption of propane and propylene in zeolite NaX at 318 K.

References

1. R. B. Eldridge, Olefin/paraffin separation technology: A review. *Ind. Eng. Chem. Res.* **32**, 2208 (1993). doi:10.1021/ie00022a002

2. K. Tanaka, A. Taguchi, J. Hao, H. Kita, K. Okamoto, Permeation and separation properties of polyimide membranes to olefins and paraffins. *J. Membr. Sci.* **121**, 197 (1996). doi:10.1016/S0376-7388(96)00182-2

3. D. J. Safarik, R. B. Eldridge, Olefin/paraffin separations by reactive absorption: A review. *Ind. Eng. Chem. Res.* **37**, 2571 (1998). doi:10.1021/ie970897h

4. M. Eddaoudi *et al*., Systematic design of pore size and functionality in isoreticular MOFs and their application in methane storage. *Science* **295**, 469 (2002). doi:10.1126/science.1067208 Medline

5. S.-I. Noro, S. Kitagawa, M. Kondo, K. Seki, A new, methane adsorbent, porous coordination polymer [CuSiF6(4,4′-bipyridine)2n]. *Angew. Chem. Int. Ed.* **39**, 2081 (2000). doi:10.1002/1521-3773(20000616)39:12<2081::AID-ANIE2081>3.0.CO;2-A

6. L. J. Murray, M. Dincă, J. R. Long, Hydrogen storage in metal-organic frameworks. *Chem. Soc. Rev.* **38**, 1294 (2009). doi:10.1039/b802256a Medline

7. N. L. Rosi *et al*., Hydrogen storage in microporous metal-organic frameworks. *Science* **300**, 1127 (2003). doi:10.1126/science.1083440 Medline

8. J.-R. Li, R. J. Kuppler, H.-C. Zhou, Selective gas adsorption and separation in metal-organic frameworks. *Chem. Soc. Rev.* **38**, 1477 (2009). doi:10.1039/b802426j Medline

9. Y.-S. Bae *et al*., Carborane-based metal-organic frameworks as highly selective sorbents for CO(2) over methane. *Chem. Commun. (Camb.)* (35): 4135 (2008). doi:10.1039/b805785k Medline

10. S. Bourrelly *et al*., Different adsorption behaviors of methane and carbon dioxide in the isotypic nanoporous metal terephthalates MIL-53 and MIL-47. *J. Am. Chem. Soc.* **127**, 13519 (2005). doi:10.1021/ja054668v Medline

11. J. W. Yoon *et al*., *Angew. Chem. Int. Ed.* **49**, 5949 (2010).

12. Z. Zhang, S. Xiang, B. Chen, Microporous metal–organic frameworks for acetylene storage and separation. *CrystEngComm* **13**, 5983 (2011). doi:10.1039/c1ce05437f

13. S.-C. Xiang *et al*., Rationally tuned micropores within enantiopure metal-organic frameworks for highly selective separation of acetylene and ethylene. *Nat. Commun.* **2**, 204 (2011). doi:10.1038/ncomms1206 Medline

14. H. Leclerc *et al*., Infrared study of the influence of reducible iron(III) metal sites on the adsorption of CO, CO2, propane, propene and propyne in the mesoporous metal-organic framework MIL-100. *Phys. Chem. Chem. Phys.* **13**, 11748 (2011). doi:10.1039/c1cp20502a Medline

15. R. Matsuda *et al*., Highly controlled acetylene accommodation in a metal-organic microporous material. *Nature* **436**, 238 (2005). doi:10.1038/nature03852 Medline

16. E. D. Bloch *et al*., Selective binding of O2 over N2 in a redox-active metal-organic framework with open iron(II) coordination sites. *J. Am. Chem. Soc.* **133**, 14814 (2011). doi:10.1021/ja205976v Medline

17. Z. Bao *et al*., Adsorption of ethane, ethylene, propane, and propylene on a magnesium-based metal-organic framework. *Langmuir* **27**, 13554 (2011). doi:10.1021/la2030473 Medline

18. Y.-S. Bae *et al*., High propene/propane selectivity in isostructural metal-organic frameworks with high densities of open metal sites. *Angew. Chem. Int. Ed.* **51**, 1857 (2012). doi:10.1002/anie.201107534

19. A. Fürstner *et al*., Preparation, structure, and reactivity of nonstabilized organoiron compounds: Implications for iron-catalyzed cross coupling reactions. *J. Am. Chem. Soc.* **130**, 8773 (2008). doi:10.1021/ja801466t Medline

20. H. Wu, W. Zhou, T. Yildirim, High-capacity methane storage in metal-organic frameworks M2(dhtp): The important role of open metal sites. *J. Am. Chem. Soc.* **131**, 4995 (2009). doi:10.1021/ja900258t Medline

21. R. Krishna, J. R. Long, Screening metal–organic frameworks by analysis of transient breakthrough of gas mixtures in a fixed bed adsorber. *J. Phys. Chem. C* **115**, 12941 (2011). doi:10.1021/jp202203c

22. A. L. Myers, J. M. Prausnitz, Thermodynamics of mixed-gas adsorption. *AIChE J.* **11**, 121 (1965). doi:10.1002/aic.690110125

23. S. H. Hyun, R. P. Danner, Equilibrium adsorption of ethane, ethylene, isobutane, carbon dioxide, and their binary mixtures on 13X molecular sieves. *J. Chem. Eng. Data* **27**, 196 (1982). doi:10.1021/je00028a029

24. J. J. Gutiérrez-Sevillano *et al*., *J. Phys. Chem. C* **114**, 14907 (2010).

25. M. C. Das *et al*., A new approach to construct a doubly interpenetrated microporous metal-organic framework of primitive cubic net for highly selective sorption of small hydrocarbon molecules. *Chemistry* **17**, 7817 (2011). doi:10.1002/chem.201100350 Medline

26. M. G. Plaza *et al*., Propane/propylene separation by adsorption using shaped copper trimesate MOF. *Microporous Mesoporous Mater.*, published online 14 July 2011. 10.1016/j.micromeso.2011.06.024

27. L. J. Murray *et al*., Highly-selective and reversible O2 binding in Cr3(1,3,5-benzenetricarboxylate)2. *J. Am. Chem. Soc.* **132**, 7856 (2010). doi:10.1021/ja1027925 Medline

28. S. C. Reyes *et al*., U.S. Patent 12,322,364 (2009).

29. R. Krishna, J. M. van Baten, Investigating the potential of MgMOF-74 membranes for CO2 capture. *J. Membr. Sci.* **377**, 249 (2011). doi:10.1016/j.memsci.2011.05.001

30. R. Krishna, Describing the diffusion of guest molecules inside porous structures. *J. Phys. Chem. C* **113**, 19756 (2009). doi:10.1021/jp906879d

31. R. Krishna, J. M. van Baten, Maxwell–Stefan modeling of slowing-down effects in mixed gas permeation across porous membranes. *J. Membr. Sci.* **383**, 289 (2011). doi:10.1016/j.memsci.2011.08.067

32. H. Bux, C. Chmelik, R. Krishna, J. Caro, Ethene/ethane separation by the MOF membrane ZIF-8: Molecular correlation of permeation, adsorption, diffusion. *J. Membr. Sci.* **369**, 284 (2011). doi:10.1016/j.memsci.2010.12.001

33. G. A. Bain, J. F. Berry, Diamagnetic corrections and Pascal's constants. *J. Chem. Educ.* **85**, 532 (2008). doi:10.1021/ed085p532

34. R. Georges, J. J. Borras-Almenar, E. Coronado, J. Curely, M. Drillon, in *Magnetism: Molecules to Materials I: Models and Experiments*, J. S. Miller, M. Drillon, Eds. (Wiley-VCH: Weinheim, Germany, 2002), pp. 1–47.

35. O. Kahn, *Molecular Magnetism* (Wiley-VCH, New York, 1993).

36. K.-D. Liss, B. A. Hunter, M. E. Hagen, T. J. Noakes, S. J. Kennedy, Echidna: The new high-resolution powder diffractometer being built at OPAL. *Physica B* **385-386**, 1010 (2006). doi:10.1016/j.physb.2006.05.322

37. B. H. Toby, EXPGUI, a graphical user interface for GSAS. *J. Appl. Cryst.* **34**, 210 (2001). doi:10.1107/S0021889801002242

38. A. C. Larson, R. B. Von Dreele, General Structure Analysis System (GSAS), Los Alamos National Laboratory Report LAUR, 86-748 (Los Alamos National Laboratory, Los Alamos, 1994).

39. N. Lamia *et al*., Propane/propylene separation by simulated moving bed II: Measurement and prediction of binary adsorption equilibria of propane, propylene, isobutane, and 1-butene on 13x zeolite. *Sep. Sci. Technol.* **44**, 1485 (2009). doi:10.1080/01496390902775935

40. J. A. Mason, K. Sumida, Z. R. Herm, R. Krishna, J. R. Long, Evaluating metal–organic frameworks for post-combustion carbon dioxide capture via temperature swing adsorption. *Energy Environ. Sci.* **4**, 3030 (2011). doi:10.1039/c1ee01720a

41. I. G. Giannakopoulos, V. Nikolakis, Separation of propylene/propane mixtures using faujasite-type zeolite membranes. *Ind. Eng. Chem. Res.* **44**, 226 (2005). doi:10.1021/ie049508r

42. D. Dubbeldam *et al*., United atom force field for alkanes in nanoporous materials. *J. Phys. Chem. B* **108**, 12301 (2004). doi:10.1021/jp0376727

43. S. Ban, A. vanLaak, P. E. deJongh, J. P. J. M. vanderEerden, T. J. H. Vlugt, Adsorption selectivity of benzene/propene mixtures for various zeolites. *J. Phys. Chem. C* **111**, 17241 (2007). doi:10.1021/jp074918p

44. A. K. Rappé, C. J. Casewit, K. S. Colwell, W. A. Goddard, W. M. Skiff, UFF, a full periodic table force field for molecular mechanics and molecular dynamics simulations. *J. Am. Chem. Soc.* **114**, 10024 (1992). doi:10.1021/ja00051a040

45. S. L. Mayo, B. D. Olafson, W. A. Goddard, DREIDING: A generic force field for molecular simulations. *J. Phys. Chem.* **94**, 8897 (1990). doi:10.1021/j100389a010